REPORT DOCUMENTATION PAGE

Form Approved
OMB NO. 0704-0188

1. AGENCY USE ONLY (Leave Blank)	2. REPORT DATE 23 June 2003	3. REPORT TYPE AND DATES COVERED Final Report (July 2000-June 2003)

4. TITLE AND SUBTITLE Electronic Sensors for Microfluidics	5. FUNDING NUMBERS Contract No. DAAD19-00-1-0369
6. AUTHOR(S) Prof. Lydia L. Sohn	

7. PERFORMING ORGANIZATION NAME(S) AND ADDRESS(ES) Dept. of Physics, Jadwin Hall Princeton University, Princeton, NJ 08544	8. PERFORMING ORGANIZATION REPORT NUMBER P-41399-LS-000-0117-1
9. SPONSORING / MONITORING AGENCY NAME(S) AND ADDRESS(ES) U. S. Army Research Office P.O. Box 12211 Research Triangle Park, NC 27709-2211	10. SPONSORING / MONITORING AGENCY REPORT NUMBER *41399.1-LS*

12 a. DISTRIBUTION / AVAILABILITY STATEMENT Approved for public release; distribution unlimited.	12 b. DISTRIBUTION CODE DOD

13. ABSTRACT (Maximum 200 words)

The goal of this ARO/DARPA funded project is to develop a fully integrated microfluidic device that would be capable of electronically detecting specific bacterial pathogens in whole blood, and other fluids such as sputum and urine. The integrated device consists of two sensors: a microscale Coulter counter that sizds and then fractionates blood samples based on particulate size; and an on-chip high frequency spectrometer that interrogates the dielectric response of an unknown pathogen (bacteria, protozoa, or yeast) at specific frequencies. A library of frequencies corresponding to known cell types will ultimately map to the spectral response of the unknown organism, thus permitting very rapid identification of species and form (i.e. vegetative vs. spore). An integral part of the proposed work is the integration of these two sensors into a compact, microfluidic device. Crucial to the success of this integration is the utilization of microfluidic tectonics (µFT) developed by the Beebe group at the University of Wisconsin—Madison.

This grant will be re-awarded to the PI—Lydia L. Sohn—at the University of California, Berkeley (Dept. of Mechanical Engineering).

14. SUBJECT TERMS Microfluidics, electronic sensors, microscale Coulter counter, high-frequency spectrometer, pathogen, immunoassay	15. NUMBER OF PAGES 11 *of Appendices*
	16. PRICE CODE

17. SECURITY CLASSIFICATION OR REPORT UNCLASSIFIED	18. SECURITY CLASSIFICATION ON THIS PAGE UNCLASSIFIED	19. SECURITY CLASSIFICATION OF ABSTRACT UNCLASSIFIED	20. LIMITATION OF ABSTRACT UL

Enclosure 1

20030702 025

TABLE OF CONTENTS

LIST OF APPENDIXES

I. Statement of Problem Studied

The goal of this ARO/DARPA funded project is to develop a fully integrated microfluidic device that would be capable of electronically detecting specific bacterial pathogens in whole blood, and other fluids such as sputum and urine. The integrated device consists of two sensors: a microscale Coulter counter that sizes and then fractionates blood samples based on particulate size; and an on-chip high frequency spectrometer that interrogates the dielectric response of an unknown pathogen (bacteria, protozoa, or yeast) at specific frequencies. A library of frequencies corresponding to known cell types will ultimately map to the spectral response of the unknown organism, thus permitting very rapid identification of species and form (i.e. vegetative vs. spore). An integral part of the proposed work is the integration of these two sensors into a compact, microfluidic device. Crucial to the success of this integration is the utilization of microfluidic tectonics (μFT) developed by the Beebe group at the University of Wisconsin—Madison.

II. Summary of the Most Important Results

On-Chip High-Frequency Spectrometer

Our original design for the on-chip high-frequency spectrometer was a coplanar waveguide (CPW) device that could access frequencies from 100 MHz to 40 GHz (see Figure 1). This particular device consists of symmetric metal transmission lines: 40 μm-wide central strip bordered by two grounded 380 μm-wide conductors. Each metal region is an evaporated Ti/Au 50 Å/500 Å base topped with an electrodeposited gold layer (total Au thickness 1~μm). The substrate is glass, and microwave probes connect the device to a spectrum analyzer. Capacitive coupling to the fluid is achieved by encapsulating the metal lines in 1000 Å of PECVD-grown silicon nitride. PDMS-based microfluidics confines the fluid over the transmission lines.

Over the course of a year, we have well characterized this CPW device. We conclude that the electronic coupling between the device and a fluid-based sample is weak and therefore not optimal. In addition, we also conclude that there is a need for an alternative microfluidic handling system since the PDMS-based fluidics leaks often (PDMS bonds well to glass and silicon but unfortunately not to large areas of metal). Consequently, we have completely redesigned our device [1]. Figure 2 is a schematic of our new device. As shown, it is of parallel-plate geometry and the sensor is embedded within a microfluidic device.

The fabrication details of this device are as follows. We first deposit a 500 Å seed layer of gold onto two glass microscope slides. We then use photolithography to pattern the gold that is subsequently electroplated to a thickness of 4-6 μm. After reactive-ion etching the photoresist

1

The fabrication details of this device are as follows. We first deposit a 500 Å seed layer of gold onto two glass microscope slides. We then use photolithography to pattern the gold that is subsequently electroplated to a thickness of 4-6 μm. After reactive-ion etching the photoresist and removing the unplated gold with a standard iodine-based gold etchant, we align the two slides under a microscope such that the microstrip conductors overlap one another in a parallel-plate geometry (80 μm x 500 μm). We control the separation between the microstrip conductors using gold foil spacers 3–25 μm thick. The foil additionally ensures coupling between the grounds on each slide. Following alignment, we employ μFT [2] to bond the two glass slides together and to create a microfluidic channel running perpendicular to the microstrip conductors (see Figure 2). We complete the device by inserting 0.02" ID vinyl tubing through predrilled input and output holes of the device. All of our devices are designed to have a 50 Ω matched impedance and minimal insertion loss for 0.05 – 40 GHz. With these characteristics, our device sensitivity is 0.05 dB.

The electronic coupling between the two conductors in this new geometry is greater than in our previous CPW design and more importantly, leads to an enhanced sensitivity. By accessing frequencies > 20 GHz with our device, we can probe unique low-frequency vibrational or rotational modes of bio-macromolecules, since at these frequencies the counterions have fully relaxed, the dipole moment of water is rapidly decreasing, and the macroscopic distortions of macromolecules become important and are reflected in the obtained spectra. As a first demonstration, we have measured PCR products. We are able to distinguish between non-reacted primers for PCR amplification and reacted PCR products (24 amplification cycles). Figure 3 shows representative spectra of the two different DNA solutions obtained from a single device and scaled to DI water. We have obtained similar spectral features from additional devices and are currently developing a quantitative model to explain our results.

Microscale Coulter Counter

We have continually improved the sensitivity of this sensor and have recently used it as an entirely new, all-electronic technique for detecting the binding of *unlabeled* antibody-antigen pairs [3]. Our method is based on the resistive pulse technique of particle sizing [4, 5]: a particle passing through a pore displaces conducting fluid, which causes a transient increase, or pulse, in the pore's electrical resistance that in turn is measured as a decrease in current. Because the magnitude of the pulse is directly related to the diameter of the particle that produced it [5, 6], we can detect the increase in diameter of a latex colloid upon binding to an unlabeled specific antibody (see Figure 4).

Using micron-sized pores embedded in PDMS, we have successfully employed this novel technique to perform two important types of immunoassays: an inhibition assay, in which we

2

detect the presence of an antigen by its ability to disrupt the binding of antibody to the colloid; and a sandwich assay, in which we successively detect the binding of each antibody in a two-site configuration [2]. We have used the latter assay to discriminate between *Streptococcus* Group *A* bacteria vs. *Streptococcus* Group *B* bacteria (see Figure 5). We show that our technique is an order more sensitive and more than four times as fast as an agglutination assay.

The true strength of our technique is its generality: it does not rely on any functional properties of the free ligand. Thus, it can be applied to any ligand/receptor pair, provided the free ligand is large enough to produce a discernible change in the size of the colloid. Additionally, because we employ a chip-based microfluidic device, three advantages are conferred upon our system. First, because we have miniaturized the reservoirs leading to the pore, each measurement uses sub-microliter quantities of sample and can be performed within minutes. Second, we utilize common microfabrication and micro-molding techniques to make the pore, reservoirs, and electrodes. This allows for quick and inexpensive device construction. Third, using chip-based fabrication can extend the device's capabilities by permitting either future integration of our measurement with other microfluidic components such as separation units or mixers, or construction of arrays of sensors on a single chip for performing many measurements or assays in parallel.

III. Technology Transition

Currently, the Biosensors Team at the Edgewood Chemical and Biological Center is evaluating our two sensors for DoD applications.

IV. Listing of All Publications Under This Contract

A. *Peer-Reviewed Journals*

1. J. Moorthy, and D. J. Beebe, *Organic and Bio-mimetic Approaches in Designing Microfluidic Systems* , (invited) *Anal Chem*, to appear July, 2003
2. O. A. Saleh and L. L. Sohn, *Direct Detection of Antibody-Antigen Binding Using an On-Chip Artificial Pore*, Proc. Natl. Acad. Sci. **100**, 820-824 (2003).
3. O. A. Saleh and L. L. Sohn, *An Artificial Nanopore for Molecular Sensing*, NanoLetters **3**, 37-38 (2003).
4. O. A. Saleh and L. L. Sohn, *Correcting Off-Axis Effects in an On-chip Resistive Pulse Analyzer*, Rev. Sci. Inst. **73**, 4396-4398 (2002).
5. G. R. Facer, D. A. Notterman, and L. L. Sohn, *Electronic Biosensing*, appears as an invited chapter in the National Institutes of Environmental Health Sciences, National Institutes of Health, <u>Biomarkers of Environmentally Associated Disease</u>, eds. S. H. Wilson and W. A. Suk, CRC Press, 527-548 (2002).
6. O. A. Saleh and L. L. Sohn, *Quantitative Sensing of Sub-Micron Colloids Using a Microchip Coulter Counter*, Rev. Sci. Inst. **72**, 4449 (2001).
7. G. R. Facer, D. A. Notterman, and L. L. Sohn, *Dielectric Spectroscopy for Bioanalysis: 40 Hz to 26.5 GHz in a Microfabricated Waveguide*, Appl. Phys. Lett. **78**, 996 (2001).

B. *Conference Proceedings*

1. T. C. Messina, L. N. Dunkleberger, G. A. Mensing, A. Kalmbach, D. J. Beebe, R. Weiss, and L. L. Sohn, *A Novel High Frequency Sensor for Biological Discrimination*, Seventh International Conference on Miniaturized Chemical and Biochemical Analysis Systems, Micro TAS 2003, Squaw Valley, CA, October, 2003.
2. G. Mensing, D. Kim, J. Moorthy, J. Bassett, D. Eddington, and D. J. Beebe, *A Reconfigurable integrated Device for Bio assay Development*, Seventh International Conference on Miniaturized Chemical and Biochemical Analysis Systems, Micro TAS 2003, Squaw Valley, CA, October, 2003.
3. O. A. Saleh and L. l. Sohn, *A Resistive Sensing Device for Biological Solutions*, Biophysical Journal 80 (1): 637, Part 2 Jan 2001.
4. G. R. Facer, D. A. Notterman, and L. L. Sohn, *Electronic Characterization of Biological Fluid Samples: 40 Hz to 30 GHz*, Biophysical Journal 80 (1): 652, Part 2 Jan 2001
5. L. L. Sohn, O. A. Saleh, G. R. Facer, A. Beavis, R. S. Allan, and D. A. Notterman, *Capacitance Cytometry: Measuring Biological Cells One-by-One*, Biophysical Journal 80 (1): 639, Part 2 Jan 2001.

C. *Papers Presented at Meetings But Not Published in Conference Proceedings*

1. O. A. Saleh and L. L. Sohn, *Adding Biological Specific to a Resistive Pulse Sensor*, American Physical Society Annual March Meeting 2003.
2. L. L. Sohn, L. N. Dunkleberger, G. Mensing, D. J. Beebe, *Electronic Biosensing of Cells*, American Physical Society Annual March Meeting 2003.
3. L. L. Sohn, *Molecular Sensing Using an Articial Lateral Nanopore*, Invited Paper, American Vacuum Society Topical Conference: Understanding and Operating in Threat Environments, Monterey, CA May 2002.
4. L. L. Sohn, *Peering in the Life of a Cell: Developing Electronic Techniques to Identify Proteins In Vivo*, Invited Paper, American Physical Society Annual March Meeting 2002.
5. O. A. Saleh, *Molecular Sensing with an Artificial Pore*, Invited Paper, American Physical Society Annual March Meeting 2002.
6. G. R. Facer, U*sing Permittivity Measurements to Probe Biological Solutions*, American Physical Society Annual March Meeting 2002.
7. L. L. Sohn, *Nanoelectronic Sensing—From Single Cells to Single Molecules*, Invited Paper, American Chemical Society Prospectives, Biological Applications of Nanotechnology, Berkeley, CA June 2002.
8. L. L. Sohn, *Capacitance Cytometry: Measuring Single Cells One-by-One*, Int'l. Conference on Electronic Interactions in DNA—UCLA September 2001.
9. O. A. Saleh and L. L. Sohn, *On-Chip Resistive Sensing of Submicron Particles*, American Physical Society Annual March Meeting 2001.
10. O. A. Saleh and L. L. Sohn, *Charge-Sensitive Detection of Single Submicron Particles in Solution*, American Physical Society Annual March Meeting 2000.
11. G. R. Facer, L. L. Sohn, D. A. Notterman, *Electronic Spectroscopy of Biological Solutions in Microfluidic Devices*, American Physical Society Annual March Meeting 2000.
12. L. L. Sohn, O. a. Saleh, G. R. Facer, J. D. Carbeck, A. Beavis, and D. A. Notterman, *Detecting DNA in Eukaryotic Cells Using Using an Integrated Microfluidics Electronic Sensor*, American Physical Society Annual March Meeting 2000.
13. L. L. Sohn, *A Micro-Electronic Flow Cytometer*, XX Congress for the Int'l. Soc. for Analytical Cytology, Montpellier, France May 2000.

V. List of All Participating Scientific Personnel Showing Adv. Degrees Earned While Employed on the Project

O. A. Saleh, Ph.D. Princeton University (January, 2003)
   Thesis title: A Novel Resistive Pulse Sensor for Biological Measurements

VI. List of Scientific Personnel Supported on the Project

1. O. A. Saleh, graduate student (Princeton University)
2. LaRue Dunkleberger, research associate (Princeton University)
3. Wonje Jeong, graduate student (Univ. of Wisconsin-Madison)
4. Swomitra "Bobby" Mohanty (Univ. of Wisconsin-Madison)
5. Dr. Glennys A. Mensing, Associate Scientist (Univ. of Wisconsin-Madison)

VII. Report of Inventions

1. Co-planar Waveguide Used to Determine the Electrical Properties of Biological Solutions," L. L. Sohn, G. R. Facer, and D. A. Notterman—filed for a US Letters Patent Nov. 2000.
2. Protein & Macromolecular Identification & Separation on a Chip," L. L. Sohn and O. A. Saleh—filed for a US Letters Patent, Jan. 2001

Currently, Fluidigm Corp. has entered a licensing agreement with Princeton University for the above technologies.

VIII. Bibliography

1. T. C. Messina, L. N. Dunkleberger, G. A. Mensing, A. Kalmbach, D. J. Beebe, R. Weiss, and L. L. Sohn, *A Novel High Frequency Sensor for Biological Discrimination*, Seventh International Conference on Miniaturized Chemical and Biochemical Analysis Systems, Micro TAS 2003, Squaw Valley, CA, October, 2003.
2. C. Khoury, G. A. Mensing, and D. J. Beebe, *Lab on a Chip* **2**, 50 (2002).
3. O. A. Saleh and L. L. Sohn, *Direct Detection of Antibody-Antigen Binding Using an On-Chip Artificial Pore*, Proc. Natl. Acad. Sci. **100**, 820-824 (2003).
4. W.H. Coulter. United States Patent No. 2,565,508 (20 Oct. 1953).
5. R.W. Deblois, C.P. Bean, *Rev. Sci. Instrum.* **41**, 909 (1970).
6. O. A. Saleh and L. L. Sohn, *Quantitative Sensing of Sub-Micron Colloids Using a Microchip Coulter Counter*, Rev. Sci. Inst. **72**, 4449 (2001).
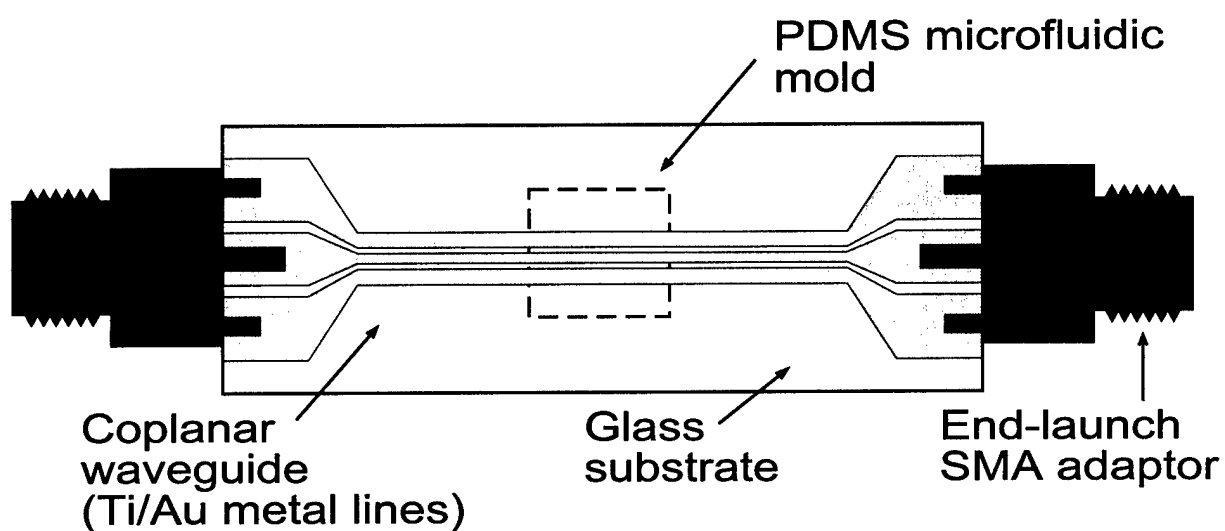
Figure 1: Coplanar waveguide (CPW) device, showing the Ti/Au wave guide (not to scale) and microfluidic handling system. Across the cenra portion, the inner line width is 40 μm, outer line widths 380 μm, and the inner-outer separation is 7 μm. Total substrate length is 34 mm.

(a)

Bottom Slide
25 X 50 X 1 mm

Top Slide
25 X 45 X 0.2 mm

Composite

HF etch to
expose leads

Drilled holes
for channel

Gold foil spacers

Microfluidic
channel

+ = Exposed leads

(b)

Gold ground
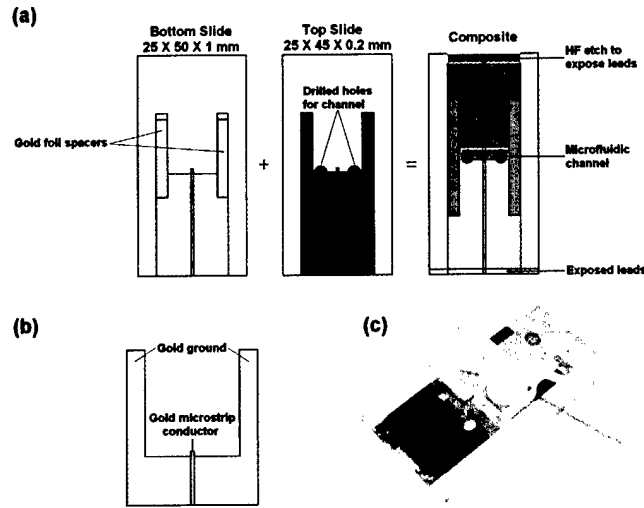
Gold microstrip
conductor

(c)

Figure 2: The modified high-frequency electronic biosensor we have developed. (a) Microfluidic tectonics is used to bond two glass slides that are previously aligned and to create a microfluidic channel perpendicular to and between the two microstrip conductors. The channel height is defined by the gold foil spacer and ranges from 3 to 25 μm; (b) An expanded view of ground and microstrip conductor. The microstrip is 80 μm wide and extends 300 μm beyond the grounds. A 20 μm gap separates the microstrip from the grounds and the top and bottom grounds overlap ~200 μm; (c) The completed device is symmetric and fluid may flow in either direction.
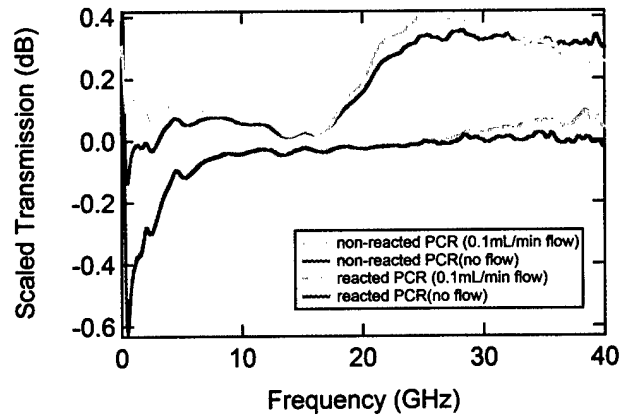

Figure 3: Transmission of non-reacted PCR primers and reacted PCR products scaled to DI water. The spectra correspond to both static and dynamic fluid flow through the microfluidic channel.
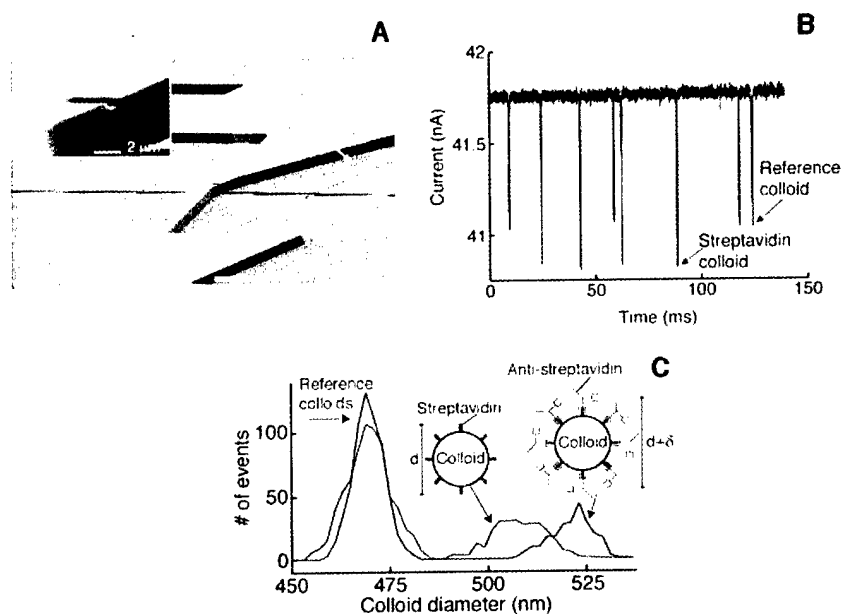
7

Figure 4: (a) SEM photo of a microscale Coulter counter in quartz. **(b)** A typical measurement of the current across the sensor as different colloids pass through it. Each downward pulse corresponds to a single colloid transiting the pore. **(c)** A histogram showing the distribution of colloid diameters measured from a solution that contains only reference and streptavidin colloids (green line), and a solution that contains both types of colloids and 0.1 mg/mL of monoclonal anti-streptavidin antibody (red line). The specific binding of anti-streptavidin to the streptavidin colloids produces a clear increase in the diameter of the colloids.
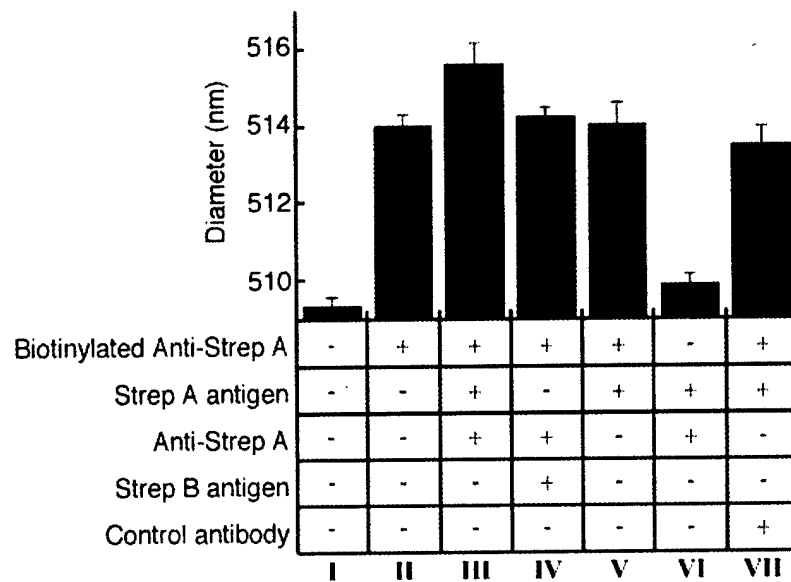
Figure 5: Summary of the mean colloid diameters measured when forming an antibody-antigen-antibody 'sandwich' on the colloid surface. All solutions contain the reference and streptavidin colloids in a 0.5x PBS buffer (pH 7.3), along with additional components as indicated by the '+' in the column below the plotted bar. Column I indicates the measured diameter of the 'bare' streptavidin colloid. We measure a ~ 5 nm increase (column II) in diameter after conjugating a biotinylated antibody (biotinylated anti-Streptococcus Group A) to the streptavidin coated colloids. A further increase of ~1.6 nm is seen (column III) when adding both extract from a culture of Streptococcus Group A and a secondary antibody specific to that antigen (unlabeled anti-Streptococcus Group A); this increase indicates the formation of the sandwich on the colloid surface. The specificity of the configuration is shown by the lack of an increase in diameter when adding extract from a culture of Streptococcus Group B (which is not bound by either antibody) in place of the Group A extract (column IV), or an irrelevant antibody in place of the specific secondary antibody (column VII). When adding the specific antigen and secondary antibody to unconjugated colloids (column VI), we measure no significant diameter increase, indicating that non-specific adhesion of antigen-secondary antibody complexes are not the cause of the diameter increase seen in column III. Finally, when adding the specific antigen alone to the conjugated colloids (column V), we see no increase in diameter, indicating that the diameter increase in column III is primarily due to the binding of the secondary antibody.

9

Biomarkers
of
ENVIRONMENTALLY ASSOCIATED DISEASE

Technologies, Concepts, and Perspectives

Samuel H. Wilson, M.D.
William A. Suk, Ph.D., M.P.H.

LEWIS PUBLISHERS

Visit the CRC Press Web site at www.crcpress.com

chapter thirty-six

Electronic biosensing

G.R. Facer, O.A. Saleh, D.A. Notterman, and L.L. Sohn

Contents

Abstract Analysis of fluid samples in the biosciences has traditionally relied on chemical and optical detection techniques.[1-3] While these techniques provide diverse and fundamental information, they have a number of disadvantages which prevent their universality. For instance, most samples must be chemically altered prior to analysis; photobleaching can place a time limit on optically probing fluorophore-tagged samples; and elaborate and expensive optical apparatus (external or integrated) is frequently required. Given these drawbacks, one poses the following question: "What alternatives to chemical and optical detection are there for bioanalysis?"

In this chapter, we suggest that electronic detection may be the answer to this question. As we will demonstrate, purely electronic techniques can probe a sample and its chemical environment directly without modification or amplification over a range of time scales. In addition, we will also demonstrate that electronic detection is ideally suited for micro total analytical systems (μ-TAS), or "lab-on-a-chip" microfluidic devices[4] as current micro- and nanofabrication techniques can produce compact, robust, and low-cost electronic sensors directly on a microfluidic chip, thus obviating the need for external detectors. We describe in detail three electronic detection techniques: capacitance cytometry,[5] dielectric spectroscopy,[6] and resistive sensing.[6a] We have developed these in our laboratory to demonstrate the power of elec-

tronic sensing in biological systems. While it is still in its infancy, electronic biosensing has already shown that it is well suited to many detection and monitoring applications in biology.

I. Capacitance cytometry

The electrical properties of biological cells are of great interest, as they can provide opportunities to develop novel, rapid assays for disease[7] and integrated hybrid chips for electronics.[8,9] Previous electrical studies of cells have focused on external macroscopic properties, such as cell membrane responses or volume, and have primarily reflected those of large ensembles of cells.[10,11] In this section, we describe capacitance cytometry, which we have recently developed and allows us to investigate some of the internal properties of individual cells.[5] Capacitance cytometry can quantify the DNA content of single eukaryotic cells from a diverse set of organisms, ranging from yeast to mammals. In addition, it can be employed as an assay for abnormal changes in DNA content, such as are frequently encountered in neoplastic cells. By monitoring the DNA content of populations of cells with this technique, one can produce a profile of their cell-cycle kinetics. Thus, capacitance cytometry may serve as a medical diagnostic tool whose low-detection limit of just one cell can identify the presence of malignancy in small quantities of tissue, and without special processing.

Though able to interrogate cells one by one, standard laser flow cytometry requires sample preparation such as sample staining or manipulation of cells. In contrast, our electronic technique requires no special preparation. Thus, capacitance cytometry has the potential to be simpler, faster, and less expensive than standard laser flow cytometry.

The fundamental basis of capacitance cytometry is an AC capacitance measurement. This extremely sensitive yet robust electronic technique allows one to probe the polarization response of a wide range of materials — organic and inorganic — to an external electric field. In the past, capacitance measurements have been used to identify and investigate a number of different materials in bulk.[12] More recently, it has been used to investigate ensembles of biological cells, determining cell size and cellular membrane capacitance, in order to assay cell-cycle progression[10] and to differentiate normal and malignant white blood cells.[11] In contrast, here we employ capacitance measurements as a means of detecting and quantifying the polarization response of DNA within the nucleus of single eukaryotic cells. Since DNA is a highly charged molecule, in an applied low-frequency AC electric field its polarization response, in combination with the motion of the surrounding counterions, can be substantial.[13] We measure this response as a change in total capacitance, ΔC_T, across a pair of microelectrodes as individual eukaryotic cells suspended in buffer solution flow one by one through a microfluidic channel (Figure 36.1). Unlike a Coulter counter, which measures displaced volume as cells or particles flow through a small orifice,[14] our integrated microfluidic chip measures the polarization response of a cell as it passes

(a)

(b)
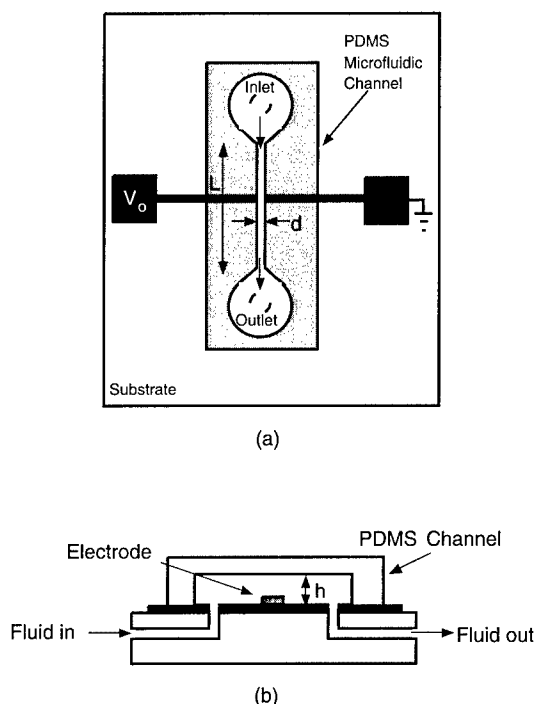
Figure 36.1 Schematic illustration of the integrated microfluidic device. (a) Top view shows the entire device, including electrode configuration, inlet and outlet holes for fluid, and the PDMS microfluidic channel. The electrodes are made of gold and are 50 μm wide. The distance d separating the electrodes is 30 μm. The width of the PDMS microfluidic channel is also d, the length L is 5 mm, and the height h is either 30 μm or 40 μm. (b) Side view along the vertical axis of the device shows a detailed view of fluid delivery. Fluid delivery is accomplished with a syringe pump at non-pulsatile rates ranging from 1 to 300 μL/hr. (From Sohn, L.L. et al., *Proc. Natl. Acad. Sci. USA*, 97, 10687–10690, 2000. With permission.)

through an electric field region. The data we obtain therefore relate, at least in part, to the charge distribution within the cell.

Electronic measurements in conductive solutions often lead to complications due to charge-screening effects at the electrode-fluid interface, i.e., electrode polarization. The measurements we report here are subject to these ionic effects, a fact that prevents our interpreting absolute capacitance values. However, since electrode polarization is localized to the electrode surface (to within the Debye screening length for the solution) and remains constant for a particular device geometry, ion concentration, and applied frequency, we can determine cellular properties by comparing changes in total capacitance values among different cells passing through our device.

The fabrication of our integrated microfluidic device is a multistage process. Photolithography is first used to fabricate a pair of 50 μm-wide, gold microelectrodes, constituting the sensor, onto a glass or quartz sub-

strate. Figure 36.1a shows a schematic of the entire device. The distance separating the two electrodes is 30 μm, three times larger than the average diameter of the eukaryotic cells we examined.[1] Millimeter-sized holes are then drilled through the substrate on either side of the completed electrodes in order to provide an inlet and outlet for the fluid and cells.

Once the central device has been fabricated, we use soft lithography[15] to create a polydimethyl siloxane (PDMS) microfluidic channel. To avoid complications arising from a cell passing directly over only one electrode and to minimize the effects of electrode polarization, we chose the channel width to be the distance separating the two electrodes. In our experiments, we employed two different channel heights, $h = 30$ μm and $h = 40$ μm. The two gave quantitatively similar results, up to an overall scale factor (see below). Once we aligned and positioned the PDMS channel over the electrodes and holes (see Figure 36.1b), we used a syringe pump (KD Scientific Syringe Pump, Model KD2100) to deliver fluid to the completed device at nonpulsatile rates ranging from 1 μl/hr to 300 μl/hr.

We measure the capacitance of the completed device using a commercial capacitance bridge (Andeen Hagerling AH2500A 1kHz Ultra-Precision Capacitance Bridge). This bridge applies a voltage ($V_{rms} = 250$ mV) at a frequency of 1 kHz across the device.[2] By electrically shielding the device and controlling the temperature precisely (to within $\pm 0.05°C$), we are able to achieve noise levels of ~5 aF when the microfluidic channel is dry and 0.1–2 fF when wet.

We have used our device to compare the DNA content of individual eukaryotic cells. Since the position of such a cell along the mitotic cell cycle is strictly related to DNA content — a cell in G_0/G_1-phase has 2N DNA content, a cell in G_2/M-phase has 4N DNA content, and a cell in S-phase has between 2N and 4N DNA content — we should be able to determine the phase of an individual cell. Because DNA is a highly charged molecule, we anticipate that it will produce a change in capacitance and this change should approximately scale with the DNA content of the cell, at least at frequencies up to 1 kHz. Thus, the device response ΔC_T to a cell in G_2/M-phase should be roughly twice that in G_0/G_1-phase, as the former has twice the DNA content (4N versus 2N DNA content); the response to a cell in S-phase should be between that of the G_0/G_1–G_2/M-phases; and, the response to a hyperdiploid cell (greater than 4N DNA content) should be greater than that of either a G_0/G_1-, S-, or G_2/M-phase cell.

Mouse myeloma cells (SP2/0), a malignant cell line, were grown in suspension to a density of approximately 10^5 cells/mL. The cells were then washed in phosphate-buffered saline (PBS) solution (pH 7.4), fixed in 75% ethanol at $-20°C$ for a minimum of 24 h, washed again with PBS solution, treated with RNAase, and then washed and resuspended for storage in 75% ethanol. Standard analysis (FACScan flow cytometer, Becton Dickinson Immunocytometry Systems, San Jose, CA), following treatment with a nucleic acid probe (SYTOX® Green Nucleic Acid Stain, Molecular Probes, Eugene Oregon), showed that approximately 41% of the cells were in G_0/G_1-
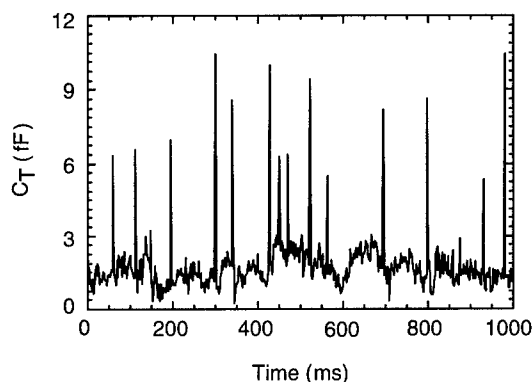
Figure 36.2 Device response over a course of 1000 ms to fixed mouse myeloma SP2/0 cells suspended in 75% ethanol and 25% phosphate buffered saline solution at 10°C. Distinct peaks are present in the data; each peak corresponds to a single cell flowing past the electrodes. The slight difference in peak widths is an artifact of the time-resolution limit of the data acquisition. The channel height of the device was 30 μm. (From Sohn, L.L. et al., *Proc. Natl. Acad. Sci. USA*, 97, 10687–10690, 2000. With permission.)

phase, 40% in S-phase, 18% in G_2/M phase of the cell cycle, and <1% were hyperdiploid.

For any given experimental run, microliters of fixed cells at a concentration of 10^5 cells/mL were injected into our device at a rate of 1 μL/hr. Using cells tagged with a fluorescent probe (SYTOX® Green Nucleic Acid Stain) we visually confirmed that, at this dilute concentration, cells flowed one by one through the microfluidic channel at an average cell velocity of ~250 μm/sec.[3] The Reynolds number was estimated to be Re~10,[2] thus ensuring that flow in the channel was laminar.

Figure 36.2 is a representative response we obtained when cells passed through a device having a channel height of 30 μm. As shown in the figure, we observe a series of sharp peaks whose amplitudes ΔC_T range from ~3 fF to ~12 fF. The individual peaks are separated by time intervals ranging from 40–100 ms. Optical observations during similar measurement runs confirm that each peak does indeed correspond to a single cell flowing past the electrodes.

A central analysis technique in flow cytometry is the DNA histogram, which provides a visual representation of the number of cells as a function of DNA content and, therefore, the proportion of cells in each phase of the cell cycle. Figure 36.3 is a histogram resulting from our capacitance measurements. As shown, there are two distinct populations of SP2/0 cells: one corresponding to 2N DNA content centered at 12.3 fF and the other corresponding to 4N DNA content centered at 23.0 fF. Based upon this capacitance histogram, we judge that approximately 48% of the cells are in G_0/G_1 phase, 30% S phase, 22% G_2/M phase, and <1% hyperdiploid. This distribution is comparable to that achieved with standard laser flow cytometry (Figure 36.3 inset).
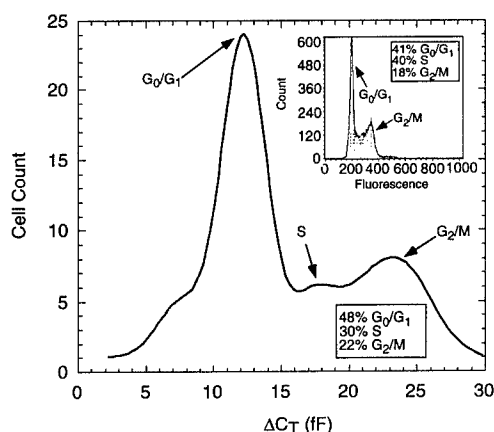
Figure 36.3 Frequency histogram of the SP2/0 cells obtained with a device of h = 30 μm, as compared to that obtained by conventional laser flow cytometry. The ungated histogram shows two major peaks, one centered at 12.3 fF, corresponding to G_0/G_1-phase, and one centered at 23.0 fF, corresponding to G_2/M-phase. The distribution of cells at capacitances less than 10 fF correspond to hypodiploid cells; the distribution of cells at capacitances greater than 27 fF are due to hyperdiploid cells. Based on the histogram obtained, we judged that approximately 48% are in G_0/G_1-phase, 30% in S phase, and 22% in G_2/M-phase. This cell cycle distribution is comparable to that obtained by conventional flow cytometry. Inset: Histogram obtained via conventional flow cytometry. The data have been gated and do not include hypo- and hyperdiploid cells. Two peaks at fluorescence channels 190 and 380 correspond to G_0/G_1- and G_2/M-phases, respectively. (From Sohn, L.L. et al., *Proc. Natl. Acad. Sci. USA*, 97, 10687–10690, 2000. With permission.)

The histogram shown in Figure 36.3 strongly suggests that our device is able to differentiate cells in different phases of the cell cycle. We can safely rule out the possibility that the measured differences in capacitance are due to cells flowing past the electrodes at different channel positions with respect to the electrodes, as we have optically confirmed that the cells flow in the center of the channel and directly between the electrodes. Since flow in the channel is laminar, we neither expect nor observe lateral motion of cells across the channel width. Over 60 devices have been tested and showed similar quantitative results, thus excluding irregularities of device fabrication.

To confirm experimentally that we are indeed differentiating cells based on their DNA content and not by size or volume (G_0/G_1 cells have half the DNA content of G_2/M cells, and are also smaller), we have also measured and compared avian red blood cells (Accurate Chemical and Scientific Corporation, Westbury, NY) to mammalian (sheep) red blood cells (Sigma Chemical Company, St. Louis, MO), both fixed with glutaraldehyde. Whereas avian red blood cells possess 2N DNA and are therefore in G_0/G_1-phase, mammalian red blood cells (the same 6–7 μm size as avian cells) contain no DNA. We observed capacitance peaks when avian cells flowed through our device, but we observed no significant peaks when interrogating the mam-
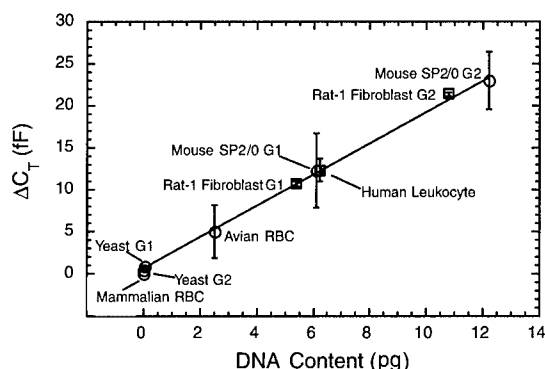
Figure 36.4 Change in capacitance ΔC_T vs. DNA content of mouse SP2/0, yeast, avian, and mammalian red blood cells. As shown, there is a linear relationship between ΔC_T and DNA content at 1 kHz frequency. Open circles correspond to data taken with a device whose channel height was 30 μm; open squares correspond to data taken with a device whose channel height was 40 μm. The 40-μm data were scaled by the ratio of the ΔC_T's obtained for mouse SP2/0 cells measured with 30-μm- and 40-μm-high channel devices (see Reference 4). All data were obtained at a temperature T = 10°C and in phosphate-buffered saline solution. (From Sohn, L.L. et al., *Proc. Natl. Acad. Sci. USA,* 97, 10687–10690, 2000. With permission.)

malian red blood cells, even after a series of experimental runs and measurements with a number of different devices. This confirms that we are indeed measuring DNA content rather than cell size or volume.

The avian red blood cells we measured have an average capacitance change, ΔC_T, of 5.0 fF. Significantly, avian red blood cells have less DNA content than SP2/0 cells and produce a smaller signal. Indeed, the ratio of observed signals of the two different types of cells (5.0 fF to 12.3 fF) is in remarkable quantitative agreement with the ratio of their DNA content (2.5 pg for *Gallus domesticus* vs. 6.1 pg for *Mus muscularis*).[16]

To determine the exact relationship between capacitance ΔC_T and DNA content, we plot ΔC_T and DNA content for the different cell types measured. As shown in Figure 36.4, a strong linear dependence exists between the two at a frequency of 1 kHz.[4] This suggests that there may be a species-independent relationship between the DNA content of eukaryotic cells and the resulting change in capacitance as these cells transit in a low-frequency electric field. Since other cellular constituents may scale with DNA content (such as nuclear histones), we cannot be certain that the entirety of the capacitance signal is derived from DNA. However, the relationship between DNA content and ΔC_T holds across cells of the four species (yeast, mouse, rat, and human) that we sampled. Since it is unlikely that all of these species have the same stoichiometric relationship between DNA and other nuclear and cytoplasmic constituents, the most likely explanation for the linear relationship between DNA content and capacitance signal is that the latter is strictly a function of the former. On an operational basis, at least, the rela-

tionship appears to be sufficiently durable to allow prediction of DNA content on the basis of ΔC_T.

Indeed, by using capacitance cytometry, we are able to detect progressive alterations in DNA content. Thus, Rat-1 rodent fibroblast cells were synchronized in the G_0/G_1-phase of the cell cycle by placing them in serum-depleted media (containing 0.1% fetal bovine serum or FBS) for 72 h. Subsequently, these cells were again permitted to grow in a serum-replete media (containing 10% FBS). Aliquots of cells were harvested from the depleted media and at intervals following the re-addition of serum. Measurement of DNA content was performed by capacitance cytometry (using a 40-μm-high channel) and by standard laser flow cytometry. A comparison of the histograms derived from capacitance cytometry and flow cytometry (Figure 36.5) indicates that cells cultured in the depleted media (t = 0 h) are synchronized at a single value of ΔC_T (centered at 3.2 fF in the histogram), which represents G_0/G_1-phase. Twelve hours following the addition of serum, the DNA content of some cells has increased as they enter the S-phase of the cell cycle. By 21 h, most of the cells are in the S-phase, and contain an amount of DNA between G_0/G_1- and G_2/M-phase. By 30 hours, many of these cells have transited G_2/M-phase (centered at 6.4 fF), and by 48 h, the cell population once more has the appearance of an asynchronously-growing population.

In summary, we describe a new method of directly determining the DNA content of single eukaryotic cells, capacitance cytometry, that uses micro-electrodes to measure changes in capacitance as cell-bearing fluid flows through a micron-sized channel. Of particular interest, we demonstrate a tight and linear relationship between the capacitance and the DNA content of a cell, and we show that this relationship is not species-dependent (among yeast, mouse, rat, and human). That this relationship does not respect inter-species boundaries implies that the measurement, ΔC_T is dependent upon DNA content *per se* rather than upon an associated cellular constituent that scales with the content of DNA.

DNA content analysis is a core technique in examining cellular physiology. We have demonstrated that our integrated microfluidic device can replicate the DNA histograms of standard laser flow cytometry. The potential applications of this simple and economical device are numerous, ranging from the experimental enumeration of DNA content in biological model systems to the determination of aneuploidy and proportion of S-phase in clinical tumor samples. In addition to advantages in cost, size, robustness, and complexity, sample preparation for the device is quite simple, compared to laser-based flow cytometry. In the experiments reported here, cell samples were fixed in ethanol or glutaraldehyde, but such treatment is not necessary, thus opening the possibility of monitoring DNA content in living tissue, such as peripheral blood, sputum, or cerebrospinal fluid. This might be advantageous in tumor cell detection and in real-time monitoring of the effects of pharmacological agents on cell cycle and cell death. Capacitance cytometry is also uniquely suited to application in microchip-based cell sorting; current efforts in this area make use of external optical detectors.[17,18]
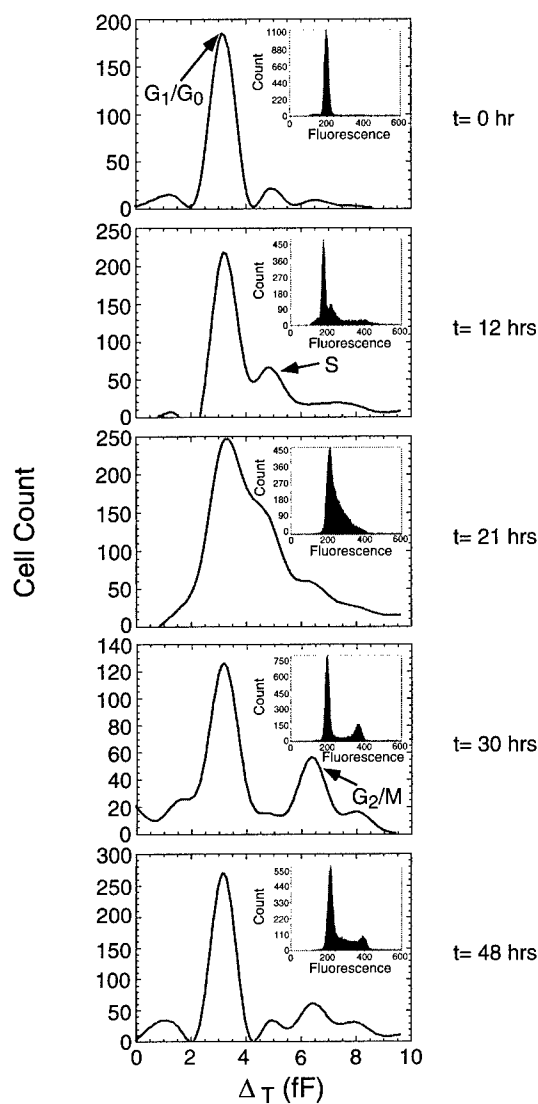
Figure 36.5 DNA Progression of Rat-1, Rodent Fibroblast Cells. Cells were G_0/G_1-arrested (t = 0 hr) and then allowed to progress through one mitotic cell cycle in synchrony. At t = 12 h, the cells are beginning to enter S-phase and at t = 21 hrs, they have fully entered this phase. At t = 30 h, the cells have entered G_2/M-phase. This is shown by the secondary peak at ΔC_T = 6.4 fF. At t = 48 hrs, the cells have completed one mitotic cell cycle and are once again in G_0/G_1-phase. The G_0/G_1-, S-, and G_2/M-phases are indicated with arrows. The data shown were taken at T = 10°C with a microfluidic channel whose height was 40 μm. Standard laser flow cytometry data for the same population of cells is shown in the insets for comparison. (From Sohn, L.L. et al., *Proc. Natl. Acad. Sci. USA*, 97, 10687–10690, 2000. With permission.)

Table 36.1   Some Responses to Electric Fields in Fluid Samples, with
Characteristic Frequency Ranges

Physical Mechanism	Characteristic Frequency (Hz)
Ionic screening at electrodes	$< 10^{-3} - 10^9$
Counterion screening around cells and macromolecules	$1 - 10^9$
Charge buildup at interfaces (membranes, etc.)	$10^3 - 10^8$
Electrorotation	$10^3 - 10^8$
Deformations of macromolecules	$> 10^6$
Rotations of solvent molecules	$10^9 - 10^{11}$ (H_2O)

The use of capacitance cytometry with these microchip-based cell sorters would further reduce the cost, size, and complexity of these devices.

II. Dielectric spectroscopy

Dielectric spectroscopy is another example of electronic detection. As opposed to capacitance cytometry, which measures capacitance at a 1 kHz frequency, dielectric spectroscopy measures permittivity as a function of frequency (from 40 Hz to 50 GHz). This direct, nondestructive, and sensitive technique can probe a system at various length scales, from centimeters to microns, with sample volumes as small as femtoliters. It, thus, provides information about the species present and the chemical environment.

In the past, a variety of research groups have applied dielectric spectroscopy across an extremely broad range of frequencies: from millihertz to tens of gigahertz. Interpreting the results of these experiments, however, has proved far from trivial. One reason for this is the number of physical processes which contribute to dielectric measurements in fluid samples. Table 36.1 below gives a partial illustration of the diverse interwoven phenomena involved.

Despite this complexity, many of the different contributions to permittivity data are well understood. For example, a simple screening theory after Cole and Cole[19] define general features in the dielectric spectra, all relating to polarization relaxations. These features are generally classified as α-, β-, or γ- dispersions. α-dispersion is the permittivity enhancement by rearrangements of small ions, including screening at the fluid interface. β-dispersion arises from distortions of cellular membranes and macromolecules. γ-dispersion is due to rotations and deformations of small, polar molecules or groups (frequently, the solvent). Access to a broad frequency range is imperative with biological samples, due to their chemical diversity.[20,21] In solution with total ionic strengths = 0.1 M, α-dispersion extends up to = 1 GHz, while β-dispersions extend from = 1 kHz[22] up to the relaxational modes of macromolecules in the infrared (THz) and beyond.

Dielectric spectra from α-, β-, and γ-dispersions have a common form[23,24]: at low frequencies, the polarization is able to closely follow the applied electric
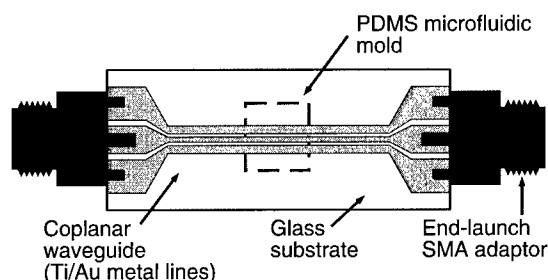
Figure 36.6 CPW device, showing the Ti/Au wave guide (not to scale) and microfluidic sample containment. Across the central portion, the inner line width is 40 μm, outer line widths 380 μm, and the inner-outer separation is 7 μm. Total substrate length is 34 mm. (From Facer, G.R., Notterman, D.A., and Sohn, L.L., *Appl. Phys. Lett.,* 78, 996–998, 2001. With permission.

field (relative permittivity $\varepsilon = \varepsilon_{lf}$); at high frequencies, applied excitations oscillate too fast for the charges to response ($\varepsilon = \varepsilon_{HF}$). Generally, $\varepsilon_{LF} >> \varepsilon_{HF}$.

We have developed a coplanar waveguide (CPW) on chip which allows us to perform dielectric spectroscopy on samples confined to a microfluidic channel or well across nearly nine orders of magnitude in frequency, from 40~Hz to 26.5~GHz.[6] Because coupling to the sample is capacitive, our CPWs allow measurements from DC to microwave frequencies, without the need for surface functionalization or chemical binding.[25] A wide range of species can, therefore, be analyzed rapidly and directly. An added feature of our CPW is that its planar geometry allows for straightforward integration with microfluidic devices.[5,26,27] Below, we discuss the fabrication of the CPW devices, and the low frequency to microwave spectra we have obtained for biomolecular solutions and cell suspensions.

A schematic diagram of our CPW devices is shown in Figure 36.6. They are symmetric metal transmission lines comprised of a 40-μm-wide central strip bordered by two grounded 380-μm-wide conductors. Each metal region is an evaporated Ti/Au 50 Å/500 Å base topped with an electrodeposited gold layer (total Au thickness 1~μm). The substrate is glass, and connection is via end-launch SMA adaptors. Capacitive coupling to the fluid is achieved by encapsulating the metal lines in 1000 Å of PECVD-grown silicon nitride. Silicone poly(dimethylsiloxane), PDMS, confines the fluid.

At frequencies below 100 MHz, the relative permittivity is obtained from the impedance Z via $\varepsilon = 1/j\omega\, Z\, C_o$, where C_o is the capacitance through the sample volume when empty and is typically ~10 fF. Z data are obtained with a Hewlett-Packard 4294A impedance analyzer (excitation amplitude 500~mV). We have confirmed that the data are free of nonlinear conductive effects. Microwave data (= 45 MHz) are phase-sensitive transmission and reflection coefficients (S-parameters) at the adaptors, obtained with a Hewlett-Packard 8510C vector network analyzer.

We have examined a variety of samples, including solutions of hemoglobin (derived from washed and lysed human red blood cells) and live *E.*
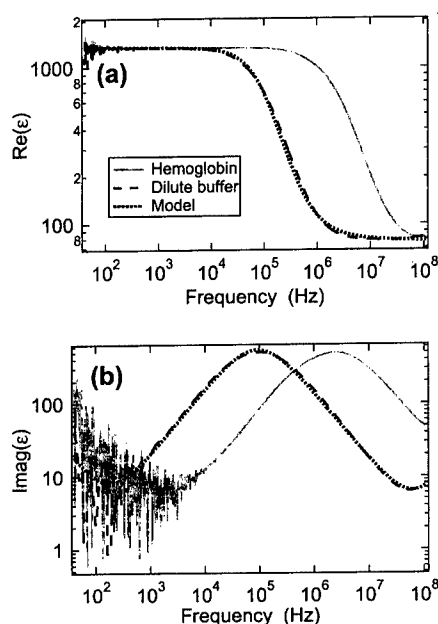
Figure 36.7 Relative permittivity data: real (a) and imaginary (b) components. Solid traces are from hemoglobin (100 µg/mL), dashed traces for Tris buffer (1 mM, pH 8), and dotted curves are Cole-Cole calculations as per Equation (36.1). (From Facer, G.R., Notterman, D.A., and Sohn, L.L., *Appl. Phys. Lett.*, 78, 996–998, 2001. With permission.)

coli suspensions. The concentration of hemoglobin is 100 µg/mL in 0.25~M Tris buffer (pH 8), and that of DNA is 500 µg/mL, in 10~mM Tris and 1~mM EDTA (pH 8) buffer. *E. coli* aresuspended in 85% 0.1 M $CaCl_2$/15% glycerol. For our measurements, we employed molded microfluidic channels and simpler enclosed wells. Results are consistent (within a scaling factor for the fluid -CPW overlap length) for sample volumes ranging from = 3 pL to = 2 0 µL. For the following discussions, we present data from capped 10 µL wells.

Figure 36.7 shows ε from 40 Hz to 110 MHz, for hemoglobin, dilute Tris buffer (concentration 1 mM, pH 8), and a Cole-Cole[19] model calculation relating ε to the angular frequency ω.

$$\varepsilon = \varepsilon_{HF} + \frac{\varepsilon_{LF} - \varepsilon_{HF}}{1 + (j\omega\tau)} - j\frac{\sigma_{LF}}{\omega} \tag{36.1}$$

Here $\varepsilon_{LF} - \varepsilon_{HF}$ is the dielectric increment, τ is a characteristic time constant, α = 1 defines the sharpness of the transition, and σ_{LF} is the DC conductivity. For the calculation in Figure 36.7, $\varepsilon_{LF} - \varepsilon_{HF} = 1340$, τ = 1.70 µs, α = 0.91, and $\sigma_{LF} = 40$ nS. A small series resistance (90W) is included in the model to fit high-frequency loss within the CPW.
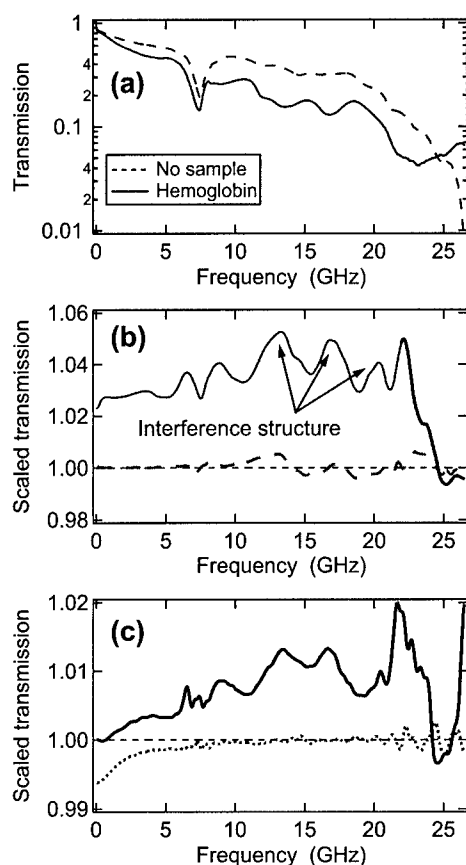
Figure 36.8 Microwave transmission data. (a) Raw data, for the cases of no sample (dotted) and a 100-μg/mL hemoglobin solution (solid). (b) Normalized data (using the respective buffers) for 100 μg/mL hemoglobin (solid trace) and 500-μg/mL phage λ-DNA (dashed), showing the difference in their microwave response. (c) Solid trace is the (buffer-normalized) response of *E. coli*, and the dotted trace is that of the Tris buffer from the hemoglobin solution (normalized using deionized H₂O). (From Facer, G.R., Notterman, D.A., and Sohn, L.L., *Appl. Phys. Lett.*, 78, 996–998, 2001. With permission.)

The spectra in Figure 36.7 show two features. First, the dielectric increment of the high-frequency transition is a constant of the measurement geometry. Second, and in contrast, the ε_{LF} to ε_{HF} transition frequency is directly proportional to the total ionic strength of the solution. As shown, the dispersion model Equation 36.1 describes the data well.

Figure 36.8 shows transmission data from 45~MHz to 26.5~GHz. In Figure 36.8a, raw transmission and reflection are shown for two control cases: a dry sample setup and deionized water. Figures 36.8b and 36.8c contain transmission data sets for hemoglobin, DNA, and live *E. coli* which have been normalized with respect to their corresponding buffers. Figure 36.8c

also shows (dotted trace) transmission data from the buffer used for hemoglobin measurements, normalized using deionized water data. This, in particular, demonstrates that even at high salt concentrations (0.25~M Tris-HCl), the microwave effects of buffer salts are limited to a monotonic decrease in transmission below 10~GHz.

Three descriptive notes should be made regarding the data. First, periodic peak and trough features (such as those marked by arrows in Figure 36.8b) are interference effects due to reflections at the SMA adaptors and the fluid itself. Second, the SMA adaptors impose the high-frequency cutoff at 26.5~GHz. Finally, reproducibility of the microwave data has been verified for three CPW devices, using several successive fluidic assemblies on each. Only the interference structure changes slightly from device to device.

The most striking aspect of the microwave data is that the transmission through the hemoglobin and bacteria specimens is higher than that through their respective buffer samples. In addition, the response due to 100 μg/mL of hemoglobin is far stronger than that for DNA even though the DNA is more concentrated (500 μg/mL). Furthermore, the hemoglobin exhibits increased transmission across a frequency range from <100 MHz to 25 GHz, which is unique among the samples measured to date (by contrast, the onset of increased transmission in the bacteria data is at ~1 GHz). The increases in transmission are not correlated to any change in reflection, indicating that there is a decrease in power dissipation within the sample. Finally, the breadth of the response implies no resonant process is at play (as is also the case for the *E. coli* data). We must, therefore, conclude that the increased transmission represents an increase in the transparency of the medium to microwaves, i.e., that these specimens are better dielectrics than water alone at this frequency. The fact that this frequency range coincides with the γ-dispersion transition in water (implying high dissipation) is most likely a contributing factor to the success of detection.

Other samples measured, for which data are not shown here (G. R. Facer, D. A. Notterman, and L. L. Sohn, unpublished), include collagen, bovine serum albumin, and ribonucleic acid solutions. These macromolecule solutions exhibit behavior highly similar to that of the DNA in Figure 36.8b (i.e., with the 10–20 GHz interference features present) and not to that of the buffer solution. This raises the possibility that the strength and shape of the interference features are more sensitive to the presence of macromolecules and their counterion clouds than just to simple salts. Again, it is reasonable to conclude that this frequency range is significant due to the γ-dispersion of water. The reason for the strength of transmission enhancement by hemoglobin, compared to that by nucleic acids or other proteins, is yet to be confirmed, but we hypothesize that it associated with the activity of the central heme complex.

In summary, we have developed CPW devices which allow us to perform dielectric spectroscopy on small volumes of biological samples confined with a microfluidic channel or well. These devices yield permittivity spectra across an exceptionally broad range of frequencies: from 40 Hz to 26.5 GHz

thus far. Neither chemical treatment nor surface activation is required. By combining transmission line design with robust thin-film insulation, sensitivity to sample properties can be achieved in low- and high-frequency regimes within a single device.

III. Resistive sensing in artificial nanopores

While we have demonstrated in the previous two sections that AC measurements are effective in detecting and quantifying biological systems in solution, we show here that simple DC measurements are just as effective, especially when quantitative measurements of the size and concentration of nanoscale particles are critical for studies of colloidal and macromolecular solutions. Traditionally, sizing is accomplished through ultracentrifugation, chromatography, gel electrophoresis,[28] or dynamic light scattering.[29] We have developed[6a] an alternative sizing method based on the Coulter technique of particle sensing.[30] Coulter counters typically consist of two reservoirs of particle-laden solution separated by a membrane and connected by a single pore through that membrane. By monitoring changes in the electrical current through the pore as individual particles pass from one reservoir to another, a Coulter counter can measure the size of particles whose dimensions are on the order of the pore dimensions. Though this method has long been used to characterize cells several microns in diameter,[31,32] its relative simplicity has led to many efforts to employ it to detect nanoscale particles[33–36] including viruses.[37]

Here, we describe the first working realization of a Coulter counter on a microchip. Our device, fabricated on top of a quartz substrate using standard microfabrication techniques, utilizes a four-point measurement of the current through the pore. We are able to control the pore dimensions precisely, which we can easily measure using optical and atomic force microscopies. Knowing the exact pore dimensions allows us to predict quantitatively the response of the device to various sized particles. We have fabricated pores with lateral dimensions between 400 nm and 1 µm and used them to detect latex colloidal particles as small as 87 nm in diameter. Furthermore, we demonstrate the ability of the device to detect ~500 nm diameter colloids with a resolution of ±10 nm. The device has numerous applications in sizing and separating nanoscale particles in solution and is easily integrated with other on-chip analysis systems.

Our device, shown in Figure 36.9a, is fabricated in multiple stages. Each stage consists of lithographic pattern generation, followed by pattern transfer onto a quartz substrate using either reactive ion etching (RIE) or metal deposition and lift-off. The first stage is the fabrication of the pore. A line is patterned on the substrate using either photolithography (PL) for line widths = 1 µm, or electron-beam lithography (EBL) for line widths between 100 and 500 nm, and then etched into the quartz using a CHF$_3$ Ri.e., The substrate subsequently undergoes a second stage of PL and RIE to define two reservoirs that are 3.5 µm deep, separated by 10 µm, and connected to each other by the previously defined channel. The length of the pore is defined in this
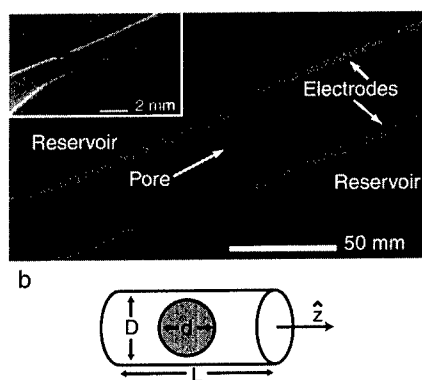
Figure 36.9 (a) Scanning electron micrograph of our microchip Coulter counter. The 3.5-m deep reservoirs and the inner Ti/Pt electrodes, which control the voltage applied to the pore but pass not current, are only partially shown. The outer electrodes, which inject current into the solution, are not visible in this image. The inset shows a magnified view of this device's pore, which has dimensions 5.1 x 1.5 x 1.0 µm.[3] (b) A schematic diagram of a spherical particle of diameter d in a pore of diameter D and length L. (From Saleh, O.A. and Sohn, L.L., *Rev. Sci. Inst.*, 72, 4449–4451, 2001.)

second stage by the separation between the two reservoirs. The final stage consists of patterning four electrodes across the reservoirs, followed by two depositions of 50 Å/250 Å Ti/Pt in an electron-beam evaporator with the sample positioned 45 degrees from normal to the flux of metal to ensure that the electrodes are continuous down both walls of the reservoirs.

The device is sealed on top with a silicone-coated (Sylgard 184, Dow Corning Corp.) glass coverslip before each measurement. Prior to sealing, the silicone and the substrate are oxidized in a dc plasma to insure the hydrophilicity[38] of the reservoir and pore and to strengthen the seal[39] to the quartz substrate. After each measurement, the coverslip is removed and discarded and the substrate is cleaned by chemical and ultrasonic methods.[5] Thus, each device can be reused many times.

We have measured solutions of negatively charged (carboxyl-coated) latex colloids (Interfacial Dynamics, Inc.), whose diameters range from 87 nm to 640 nm. All colloids were suspended in a solution of 5x concentrated TBE buffer with a resistivity of 390 Ω-cm and pH 8.2. To reduce adhesion of the colloids to the reservoir and pore walls, we added 0.05% v/v of the surfactant Tween 20 to every solution. The colloidal suspensions were diluted significantly from stock concentrations to avoid jamming of colloids in the pore; typical final concentrations were ~108 particles/mL. The pore and reservoirs were filled with solution via capillary action.

The sensitivity of a Coulter counter relies upon the relative sizes of the pore and the particle to be measured. The resistance of a pore R_p increases by δR_p when a particle enters since the particle displaces conducting fluid. δR_p can be estimated[32] for a pore aligned along the z-axis (see Figure 36.10b) by
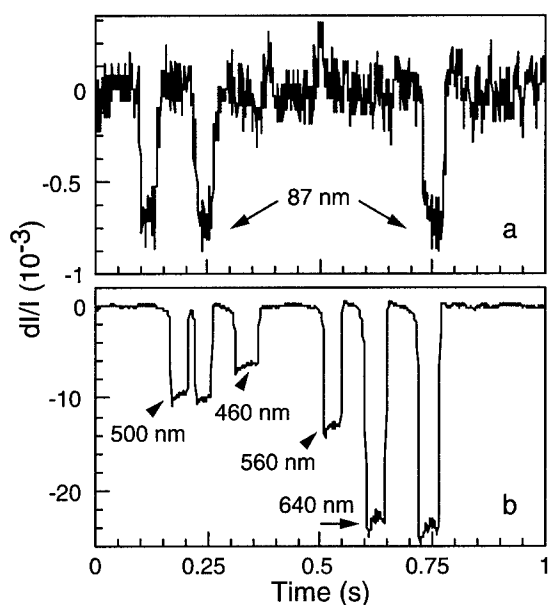
Figure 36.10 Relative changes in baseline current $\delta I/I$ vs. time for (a) monodisperse solution of 87 nm diameter latex colloids measured with an EBL-defined pore of length 8.3 μm and cross section 0.16 μm,[2] and (b) a polydisperse solution of latex colloids with diameters 5460 nm, 500 nm, 560 nm, and 640 nm measured with a PL-defined pore of length 9.5 μm and cross section 1.2 μm.[2] Each downward current pulse represents an individual particle entering the pore. The four distinct pulse heights in (b) correspond as labeled to the four different colloid diameters. (From Saleh, O.A. and Sohn, L.L., *Rev. Sci. Inst.*, 72, 4449–4451, 2001.)

$$\delta R_p = \rho \int \frac{dz}{A(z)} - R_p \qquad (36.2)$$

where $A(z)$ represents the successive cross sections of the pore containing a particle, and ρ is the resistivity of the solution. For a spherical particle of diameter d in a pore of diameter D and length L, the relative change in resistance is

$$\frac{\delta R_p}{R_p} = \frac{D}{L}\left[\frac{\arcsin(d/D)}{(1-(d/D)^{1/2}} - \frac{d}{D}\right] \qquad (36.3)$$

Equations. 36.2 and 36.3 assume that the current density is uniform across the pore and, thus, is not applicable for cases where the cross section $A(z)$ varies quickly, i.e., when $d \ll D$. For that particular case, Deblois and Bean[33] formulated an equation for δR_p based on an approximate solution to the Laplace equation:

$$\frac{\delta R_p}{R_p} = \frac{d^3}{LD^2}\left[\frac{D^2}{2L^2} + \frac{1}{\sqrt{1+(D/L)^2}}\right]F\left(\frac{d^3}{D^3}\right) \qquad (36.4)$$

where $F(d^3/D^3)$ is a numerical factor that accounts for the bulging of the electric field lines into the pore wall. When employing Equation 36.4 to predict resistance changes, we find an effective value for D by equating the cross-sectional area of our square pore with that of a circular pore.

If R_p is the dominant resistance of the measurement circuit, then relative changes in the current I are equal in magnitude to the relative changes in the resistance, $|\delta I/I| = |\delta R_p/R_p|$, and Equations 36.3 and 36.4 can be directly compared to measured current changes. This comparison is disallowed if R_p is similar in magnitude to other series resistances, such as the electrode/fluid interfacial resistance, R_{eff} or the resistance R_u of the reservoir fluid between the inner electrodes and the pore. We completely remove R_{eff} from the electrical circuit by performing a four-point measurement of the current (see Figure 36.9a). We minimize R_u by placing the inner electrodes close to the pore (50 μm away on either side), and by designing the reservoir with a cross section much larger than that of the pore. For a pore of dimensions 10.5 μm by 1.04 μm² we measured $R_p = 36$ MΩ, in good agreement with the 39 MΩ value predicted by the pore geometry and the solution resistivity. This confirms that we have removed R_u and R_{eff} from the circuit.

Figure 36.10 shows representative data resulting from measuring a monodisperse solution of colloids 87 nm in diameter with an EBL-defined pore (Figure 36.10a), and from measuring a polydisperse solution containing colloids of diameters 460 nm, 500 nm, 560 nm, and 640 nm with a PL-defined pore (Figure 36.10b). Each downward current pulse in Figure 36.10, corresponds to a single colloid passing through the pore.[6] For the data shown, 0.4 V was applied to the pore. In other runs, the applied voltage was varied between 0.1 and 1 V to test the electrophoretic response of the colloids. We found that the width of the downward current pulses varied approximately as the inverse of the applied voltage, as is expected for simple electrophoretic motion.

Figure 36.11 shows a histogram of ~3000 events measured for the polydisperse solution. The histogram shows a clear separation between the pore's response to the differently-sized colloids. The peak widths in Figure 36.11 represent the resolution of this device, which we find to be ±10 nm in diameter for the measured colloids. This precision approaches the intrinsic variations in colloid diameter of 2–4%, as given by the manufacturer. In this run, the maximum throughput was 3 colloids/s, a rate easily achievable for all of our samples. Event rates are limited by the low concentrations needed to avoid jamming.

We used a device whose pore size was 10.5 μm by 1.04 μm² to measure colloids ranging from 190 nm to 640 nm in diameter. Figure 36.12 shows the comparison between the measured mean pulse heights and those predicted by Equations. 36.3 and 36.4. As shown, there is excellent agreement between the measured and calculated values, with the measured error insignificant
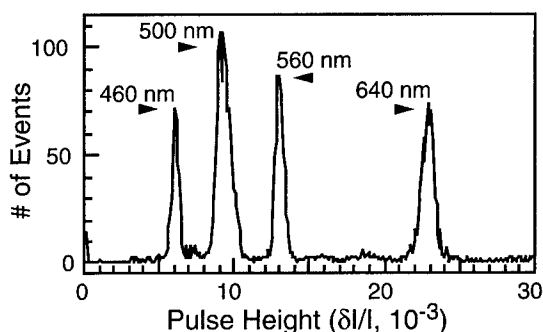
Figure 36.11 A histogram of pulse heights resulting from measuring the polydisperse solution shown in Figure 37.10b. The resolution for this particular device ±10 nm in diameter for the particles measured. (From Saleh, O.A. and Sohn, L.L., *Rev. Sci. Inst.*, 72, 4449–4451, 2001.)
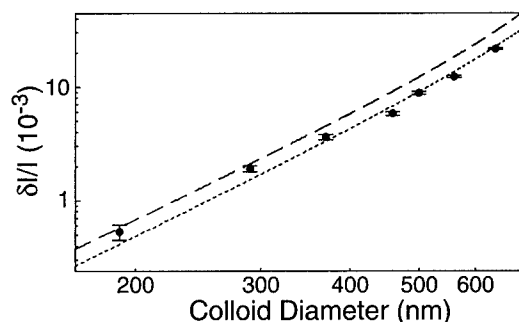
Figure 36.12 Comparison of measure $\delta I/I$ values (circles) to those predicted by Equation 36.3 (dotted line) and Equation 36.4 (dashed line). The measured data were taken over several runs on a single PL-defined pore of length 10.6 μm and cross section 1.04 μm.² Error bars for the larger colloid sizes are obscured by the size of the plotted point. AS the colloid diameter increases, there is a transition from agreement with Equation 36.4 to Equation 36.3. This reflects the fact that the derivation of Equation 36.4 assumes the colloid diameter d is much less than the pore diameters D; conversely Equation 36.3 relies on an assumption that holds only as d approaches D, and breaks down for smaller colloids. (From Saleh, O.A. and Sohn, L.L., *Rev. Sci. Inst.*, 72, 4449–4451, 2001.)

compared to the range of pulse heights. In addition, the measurements more closely follow Equation 36.4 for small d and Equation 36.3 for larger D, as was anticipated in the derivation of those equations.

In summary, we have demonstrated a microchip Coulter counter that behaves in a quantitatively predictable manner, and detects particles as small as 87 nm in diameter. The ease of device fabrication allows us to decrease the pore size, and thus decrease the detectable particle size. For example, by extending our use of EBL, we can produce pore diameters of <100 nm. Assuming a pore length of 2 μm and a current sensitivity similar to that

already achieved, such a pore could detect particles <30 nm in diameter, the length scale of many biological macromolecules. The strength of our device in size-based separation could then be utilized to study the fractionation of mixtures of large proteins or DNA molecules[6a] (O. A. Saleh and L. L. Sohn, submitted for U. S. Patent 2000).

IV. Summary

A wide range of microfluidic chips has recently been developed for detection of biological systems.[4] A fundamental component of such chips is the detector, and in many applications, multiple detectors are required. Currently, optical detection is the most commonly employed detection scheme. As an example, Mathies et al.,[4] have developed an array capillary electrophoresis system that uses an off-chip confocal scanning system. As in many microchip applications, this optical detection system is off-chip. Only Burns et al.,[40] has successfully incorporated an optical detector on-chip; however, this achievement has not been with ease nor has it been demonstrated to be easily expandable to parallel arrays of optical detectors.

Equally significant, many analytes of interest are neither inherently fluorescent nor easily tagged with artificial fluorophores. Consequently, a number of groups are investigating an electrochemical detector consisting of multiple electrodes that are located inside microchannels for measuring electrochemical potentials.[4] Like the optical detection scheme, this detector is also limiting because the electrodes erode with time.

Given these limitations in analyte detection for existing microfluidic chips, it is clear that an alternative, cost-effective technology is needed. In this chapter, we have suggested that electronic techniques can measure directly the unique intrinsic properties of analytes. The ability to detect the solid-state properties of biological samples is advantageous to other forms of microchip sensing as little sample preparation, such as those required by optical detection, is needed. The electronic sensors we have presented here are all based on current integrated circuit technology. As such, fabricating arrays of sensors on a microfluidic chip can be easily and cheaply accomplished. The cost per chip is estimated to be $0.50; the total cost of a system (with interfacing electronic and computer) ~$3000. Overall, these chips are compact and rugged, thus making on-site or in-the-field deployment more than feasible.

References

1. Nie, S. and Zare, R.N., Optical detection of single molecules, *Annu. Rev. Biophys. Biomol. Struct.*, 26, 567–596, 1997.
2. Weiss, S., Fluorescence spectroscopy of single molecules, *Science*, 283, 1676–1683, 1999.
3. MacBeath, G. and Schreiber, S.L., Printing proteins as microarrays for high-throughput function determination, *Science*, 289, 1760–1763, 2000.

4. Jed Harrison, D. and van den Berg, A., Eds., *Micro Total Analysis Systems '98*, Banff, Canada, 13–16 October, 1998.

5. Sohn, L.L. et et al., Capacitance cytometry: measuring biological cells one by one, *Proc. Natl. Acad. Sci. USA*, 97, 10687–10690, 2000.

6. Facer, G.R., Notterman, D.A., and Sohn, L.L., Dielectric spectroscopy for bioanalysis: from 40 Hz to 26.5 GHz in a microfabricated waved guide, *Appl. Phys. Lett.*, 78, 996–998, 2001.

6a. Saleh, O.A. and Sohn, L.L., Quantitative sensing of nanoscale colloids using a microship Coulter counter, *Rev. Sci. Inst.*, 72, 4449–4451, 2001.

7. Ayliffe, H.E., Frazier, A.B., and Rabbitt, R.D., Electric impedance spectroscopy using microchannels with integrated metal electrodes, *IEEE J. Microelectromech. Sys.*, 8, 50–57, 1999; Huang, Y. et al., The removal of human breast cancer cells from hematopoietic CD34(+) stem cells by dielectrophoretic field-flow-fractionation, *J. Hematother. Stem Cell Res.*, 8, 481–490, 2000.

8. Fromherz, P. et al., Membrane transistor with giant lipid vesicle touching a silicon chip, *Appl. Phys.* A 69, 571–576, 1999; Vassanelli, S. and Fromherz, P., Neurons from rat brain coupled to transistors, *Appl. Phys.*, A 65, 85–88, 1997; and Maher, M.P. et al., The neurochip: a new multielectrode device for stimulating and recording from cultured neurons. *J. Neurosci. Meth.*, 87, 45–56, 1999.

9. Kawana, A.. in *Nanofabrication and Biosystems*, Hoch, H.C., Jelinski, L.W., and Craighead, H.G., Eds., Cambridge University Press, New York, 1996, pp. 258–276; Jung, D.R. et al., Cell-based sensor microelectrode array characterized by imaging x-ray photoelectron spectroscopy, scanning electron microscopy, impedance measurements, and extracellular recordings, *J. Vac. Sci. Technol.*, A 16, 1183–1188, 1998.

10. Asami, K., Gheorghiu, E., and Yonezawa, T., Real-time monitoring of yeast cell division by dielectric spectroscopy, *Biophys. J.*, 76, 3345–3348, 1999.

11. Polevaya, Y. et al., Time domain dielectric spectroscopy study of human cells, Part II: normal and malignant white blood cells, *Biochim. Biophys. Acta*, 15, 257–71, 1999.

12. Pethig, R., *Dielectric and Electronic Properties of Biological Materials*, John Wiley and Sons, Ltd., New York, 1979.

13. Takashima, S., *J. Mol. Biol.*, 7, 455–467, 1963; Bone, S. and Small, C.A., Dielectric studies of ion fluctuations and chain bending in native DNA, *Biochim. Biophys. Acta*, 1260, 85–93, 1995; and Yang, Y. et al., Dielectric response of triplex DNA in ionic solution from simulation, *Biophys. J.*, 69, 1519–1527, 1995.

14. Yen, A., *Flow Cytometry: Advanced Research and Clinical Applications*, CRC Press, New York, 1989.

15. Xia, Y., Kim, E., and Whitesides, G.M., Micromolding in capillaries: applications in microfabrication, *Chem. Mater.*, 8, 1558–1567, 1996.

16. Tiersch, T.R. and Wachtel, S.S., On the evolution of genome size of birds, *J. Hered.*, 82, 363–368, 1991; Greilhuber, J., Volleth, M., and Loidl, J., Genome size of man and animals relative to the plant Allium cepa, *J. Genet. Cytol.*, 25, 554–560, 1983.

17. Fu, A.Y. et al., A microfabricated fluorescence-activated cell sorter, *Nature Biotech.*, 17, 1109–1111, 1999.

18. Schrum, D.P. et al., Microchip flow cytometry using electrokinetic focusing, *Anal. Chem.*, 71, 4173–4177, 1999.

19. Cole, K.S. and Cole, R.H., Dispersion and absorption in dielectrics, *J. Chem. Phys.*, 9, 341, 1941.

20. Onaral, B., Sun, H.H., and Schwan, H.P., Electrical properties of bioelectrodes, *IEEE Trans. Biomed. Eng.*, 31, 827, 1984.

21. Cirkel, P.A., van der Ploeg, J.P.M., and Koper, G.J.M., Branching and percolation in lecithin wormlike micelles studied by dielectric spectroscopy, *Physica A.*, 235, 269–278, 1997.

22. Gimsa, J. and Wachner, D., A unified resistor-capacitor modes for impedance, dielectrophoresis, electrorotation, and induced transmembrane potential, *Biophys. J.*, 75, 1107–1116, 1998.

23. Schwan, H.P. and Takashima, S., Electrical conduction and dielectric behaviour in biological systems, in *Encyclopedia of Applied Physics*, Vol. 5, VCH, New York, 1993, pp. 177–200.

24. Raicu, V., Dielectric dispersion of biological matter: model combining Debye-type and "universal" responses. *Phys. Rev.*, E 60, 4677–4680, 1999.

25. Hefti, J., Pan, A., and Kumar, A., Sensitive detection method of dielectric dispersions in aqueous-based, surface-bound macromolecular structures using microwave spectroscopy, *Appl. Phys. Lett.*, 75, 1802–1804, 1999.

26. Cooper, J.M., Towards electronic petri dishes and picolitre-scale single-cell technologies, *Trends Biotechnol.*, 17, 226–230, 1999.

27. Duffy, D.C. et al., Rapid prototyping of microfluidic systems in poly(dimethylsiloxane), *Anal. Chem.*, 70, 4974–4984, 1998.

28. Alberts, B. et al., *Molecular Biology of the Cell*, Garland Publishing, Inc., New York, 1994.

29. Russel, W.B., Saville, D.A., and Schowalter, W.R., *Colloidal Dispersions*, Cambridge University Press, New York, 1989.

30. Coulter, W.H., U.S. Patent No. 2,656,508, issued 20 Oct. 1953.

31. Kubitschek, H.E., Electronic counting and sizing of bacteria, *Nature*, 182, 234–235, 1958.

32. Gregg, E.C. and David Steidley, K., Electrical counting and sizing of mammalian cells in suspension, *Biophys.J.*, 5, 393–405, 1965.

33. DeBlois, R.W. and Bean, C.P., Counting and sizing of submicron particles by the resistive pulse technique, *Rev. Sci. Instrum.*, 41, 909–913, 1970.

34. Koch, M., Evans, A.G.R., and Brunnschweiler, A., Design and fabrication of a micromachined coulter counter, *J. Micromech. Microeng.*, 9, 159–161, 1999.

35. Sun, L. and Crooks, R.M., Fabrication and characterization of single pores for modeling mass transport across porous membranes, *Langmuir*, 15, 738–741, 1999.

36. Kobayashi, Y. and Martin, C.R., Toward a molecular Coulter counter type device, *J. of Electroanalytical Chemistry*, 431, 29–33, 1997.

37. DeBlois, R.W., Bean, C.P., and Wesley, R.K.A., Electrokinetic measurements with submicron particles and pores by resistive pulse technique, *J. Colloid Interface Sci.*, 61, 323–335, 1977.

38. Fakes, D.W. et al., The surface analysis of a plasma modified contact-lens surface by SSIMS, *Surf. Interface Anal.*, 13, 233–236, 1988.

39. Chaudhury, M.K. and Whitesides, G.M., Direct measurement of interfacial interactions between semispherical lenses and flat sheets of poly(dimethylsiloxane) and their chemical derivatives, *Langmuir*, 7, 1013–1025, 1991.

40. Burns, M.A. et al., An integrated nanoliter DNA analysis, *Science*, 282, 484–487, 1998.

A Novel High-Frequency Sensor for Biological Discrimination

T. C. Messina,[1]* L. N. Dunkleberger,[1] G. A. Mensing,[2] A. S. Kalmbach[3], D. J. Beebe,[2] R. Weiss[3], and L. L. Sohn[1]

[1]*Department of Physics, Princeton University,*
[2]*Department of Biomedical Engineering, University of Wisconsin-Madison,*
[3]*Department of Electrical Engineering, Princeton University*

Keywords: dielectric spectroscopy, microfluidics, electronic biosensing

Introduction

We have developed a high-frequency electronic biosensor of parallel-plate geometry that is embedded within a microfluidic device. This novel biosensor allows us to perform dielectric spectroscopy on a variety of biological samples—from cells to molecules—in solution. Because it is purely electronic, the sensor allows for rapid characterization with no sample preparation or chemical alteration. In addition, it is capable of probing length scales from millimeters to microns over a frequency range 50 MHz to 40 GHz, and sample volumes as small as picoliters [1,2]. Our high-frequency biosensor has evolved from previous device designs based on a coplanar waveguide (CPW) geometry [2]. For our current device, we employ microfluidic tectonics (μFT) [3] to embed two microstrip conductors within a microfluidic channel. The electronic coupling between the two conductors is greater than in our previous CPW design and more importantly, leads to an enhanced sensitivity. Our utilization of μFT allows us to incorporate easily this high-frequency electronic biosensor with a variety of lab-on-a-chip architectures.

Device Description

Figure 1 is a schematic of our high-frequency electronic biosensor. We fabricate this sensor by first depositing a 500 Å seed layer of gold onto two glass microscope slides. We then use photolithography to pattern the gold that is subsequently electroplated to a thickness of 4-6 μm. After reactive-ion etching the photoresist and removing the unplated gold with a standard iodine-based gold etchant, we align the two slides under a microscope such that the microstrip conductors overlap one another in a parallel-plate geometry (80 μm x 500 μm). We control the separation between the microstrip conductors using gold foil spacers 3–25 μm thick. The foil additionally ensures coupling between the grounds on each slide. Following alignment, we employ μFT to bond the two glass slides together and to create a microfluidic channel running perpendicular to the microstrip conductors (see Figure 1). We complete the device by inserting 0.02" ID vinyl tubing through predrilled input and output holes of the device [3]. All of our devices are designed to have a 50 Ω matched impedance and minimal insertion loss for 0.05 – 40 GHz. With these characteristics, we expect a sensitivity of 0.05 dB.

Results

By accessing frequencies > 20 GHz with our device, we can probe unique low-frequency vibrational or rotational modes of bio-macromolecules, since at these frequencies the counterions have fully relaxed, the dipole moment of water is rapidly decreasing, and the macroscopic distortions of macromolecules become important and are reflected in the obtained spectra. As a first demonstration, we have measured PCR products. We are able to distinguish between non-reacted primers for PCR amplification and reacted PCR products (24 amplification cycles). Figure 2 shows representative spectra of the two different DNA solutions obtained from a single device and scaled to DI water. We have obtained similar spectral features from additional devices and are currently developing a quantitative model to explain our results. This initial demonstration of molecular differentiation using a high-frequency electronic biosensor shows the great promise of *electronic biosensing.*

* Contact: Troy C. Messina, Physics Department, Jadwin Hall, Princeton University, Princeton, NJ 08544, tel: 609.258.1765, fax: 609.258.0986, email: tmessina@princeton.edu

References
1.   K. Asami, E. Gheorghiu, and T. Yonezawa, *Biophys. J.* **76**, 3345 (1999).
2.   G. R. Facer, D. A. Notterman, and L. L. Sohn, *Appl. Phys. Lett.* **78**, 996 (2001).
3.   C. Khoury, G. A. Mensing, and D. J. Beebe, *Lab on a Chip* **2**, 50 (2002).
4.   Y. C. Shen, P. C. Upadhya, E. H. Linfield, and A. G. Davies, *Appl. Phys. Lett.* **82**, 2350 (2003).

(a)

(b)

(c)
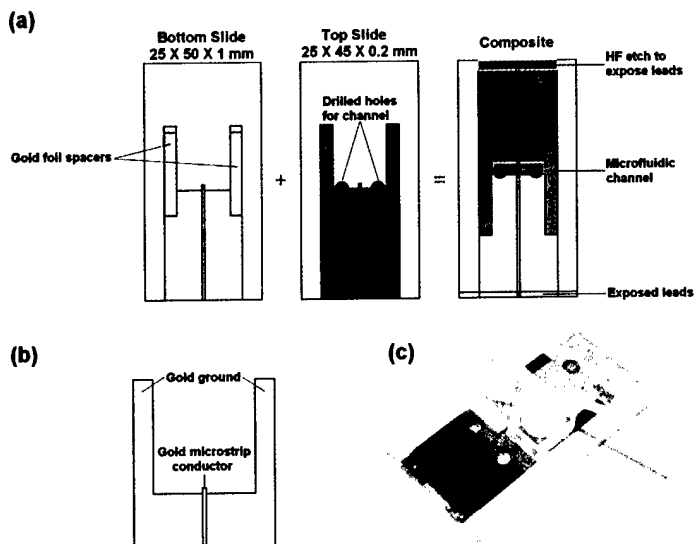
Figure 1: The high-frequency electronic biosensor we have developed. (a) Microfluidic tectonics is used to bond two glass slides that are previously aligned and to create a microfluidic channel perpendicular to and between the two microstrip conductors. The channel height is defined by the gold foil spacer and ranges from 3 to 25 μm; (b) An expanded view of ground and microstrip conductor. The microstrip is 80 μm wide and extends 300 μm beyond the grounds. A 20 μm gap separates the microstrip from the grounds and the top and bottom grounds overlap ~200 μm; (c) The completed device is symmetric and fluid may flow in either direction.

Figure 2: Transmission of non-reacted PCR primers and reacted PCR products scaled to DI water. The spectra correspond to both static and dynamic fluid flow through the microfluidic channel.

Direct detection of antibody–antigen binding using an on-chip artificial pore

Omar A. Saleh and Lydia L. Sohn*

Department of Physics, Princeton University, Princeton, NJ 08544

We demonstrate a rapid and highly sensitive all-electronic technique based on the resistive pulse method of particle sizing with a pore to detect the binding of unlabeled antibodies to the surface of latex colloids. Here, we use an on-chip pore to sense colloids derivatized with streptavidin and measure ac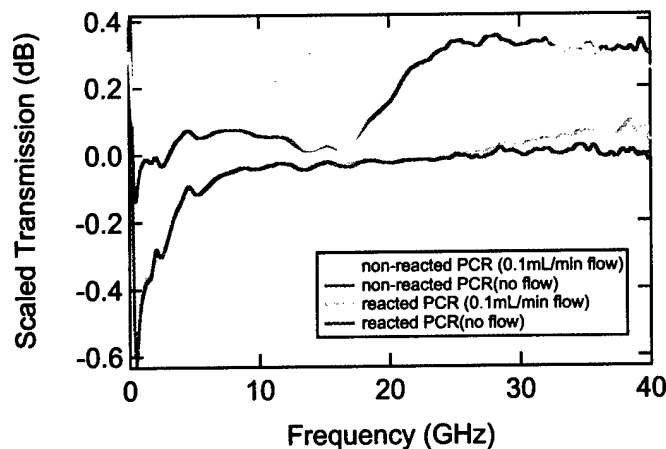curately their diameter increase on specific binding to several different types of antibodies. We show the sensitivity of this technique to the concentration of free antibody and that it can be used to perform immunoassays in both inhibition and sandwich configurations. Overall, our technique does not require labeling of the reactants and is performed rapidly by using very little solution, and the pore itself is fabricated quickly and inexpensively by using soft lithography. Finally, because this method relies only on the volume of bound ligand, it can be generally applied to detecting a wide range of ligand–receptor binding reactions.

Antibodies can be powerful and flexible tools because of their natural ability to bind to virtually any molecule and because of the modern ability to produce specific types in large quantities. These traits have led to the development of a number of important immunosensing techniques in which antibodies of a desired specificity are used to test for the presence of a given antigen (1–4). For example, RIAs have been used in clinical settings to screen for such viruses as hepatitis (5). An integral part of all immunosensing technologies is the ability to detect the binding of antibody to antigen. To accomplish this, most common immunoassays require the labeling of the antibody by using fluorescence, radioactivity, or enzyme activity. However, the need to bind chemically a label to the antibody adds to the time and cost of developing and using these technologies.

Here we report an all-electronic technique for detecting the binding of unlabeled antibody–antigen pairs. Our method is based on the resistive pulse technique of particle sizing (6): a particle passing through a pore displaces conducting fluid, which causes a transient increase, or pulse, in the pore's electrical resistance that in turn is measured as a decrease in current. This technique has been used in the past to measure the size and concentration of a variety of particles, such as cells (7), viruses (8), and colloids (9, 10). More recently, it has been used to detect single molecules (11–13) and their interactions (14). Because the magnitude of the pulse is directly related to the diameter of the particle that produced it (9, 15), we can use the resistive pulse technique to detect the increase in diameter of a latex colloid upon binding to an unlabeled specific antibody. We use this technique to perform two important types of immunoassays: an inhibition assay, in which we detect the presence of an antigen by its ability to disrupt the binding of antibody to the colloid; and a sandwich assay, in which we successively detect the binding of each antibody in a two-site configuration.

Previous particle counting-based immunoassays have used optical or electronic methods to detect the aggregates formed when the antibody crosslinks antigen-coated colloids (16–19). However, relying on crosslinking as a general binding probe is limiting because it requires a free ligand with at least two binding sites. In contrast, our method is more general, because it relies only on the added volume of bound ligand and does not place any limitations on the ligand's functionality. Although it cannot as of yet perform the kinetic analyses that surface plasmon resonance (SPR) techniques (20) are capable of, our device already represents an alternative to SPR for end-point analysis of biological reactions in that it is more rapid, inexpensive, and compact.

We perform our measurements on a chip-based microfluidic device that confers three additional advantages on our system. First, because we have miniaturized the reservoirs leading to the pore, each measurement uses submicroliter quantities of sample and can be performed within minutes. Second, we use common microfabrication and micromolding techniques (21) to make the pore, reservoirs, and electrodes. This allows for quick and inexpensive device construction. Third, using chip-based fabrication can extend the device's capabilities by permitting either future integration of our measurement with other microfluidic components (22, 23) such as separation units or mixers, or construction of arrays of sensors on a single chip for performing many measurements or assays in parallel.

Methods

Fig. 1 shows a picture of our device: a polydimethylsiloxane (PDMS) mold sealed to a glass coverslip. The PDMS mold is cast from a master (21) and contains two reservoirs (7 μm deep, 400 μm wide) connected to an embedded pore (typically 7–9 μm long and 1 μm in diameter). The glass coverslip has platinum electrodes that extend across the width of the reservoirs and are fabricated on the glass coverslip before PDMS sealing. These electrodes are used to perform the electronic measurement. We prepare both the PDMS slab and the coverslip by using standard lithographic, micromolding, and metal deposition techniques (see *Supporting Text*, which is published as supporting information on the PNAS web site, www.pnas.org). Solution is added to the reservoirs via two holes cut through the PDMS slab, and capillary action is used to initially draw the solution through both reservoirs and the pore. Pressure is applied to the access holes after loading the solution to drive the suspended latex colloids through the pore.

All solutions are mixed in 0.5× PBS, pH 7.3, and contain 0.05% Pluronics F127 surfactant (a nonionic surfactant) and 0.2 mg/ml BSA. The BSA and surfactant are added to decrease both sticking of colloids to the device walls and nonspecific adhesion of antibodies to the particles. We prepare a stock colloidal solution by mixing and twice centrifugally rinsing the colloids in the above buffer. This stock solution is then diluted by a factor of 10 and mixed with the relevant antibodies and/or antigens before each measurement. For the sandwich assay, we attach biotinylated antibody to streptavidin colloids by incubating a high concentration of the biotinylated antibody with the stock solution, then centrifugally rinsing to remove unbound molecules. Some solutions are passed through a 0.8-μm pore size filter immediately before measuring so as to remove aggregates caused by the crosslinking of the colloids by the antibody.

Once each device is loaded with the solution to be analyzed, we measure the current through the pore at constant applied DC

Abbreviation: PDMS, polydimethylsiloxane.

*To whom correspondence should be addressed. E-mail: sohn@princeton.edu.
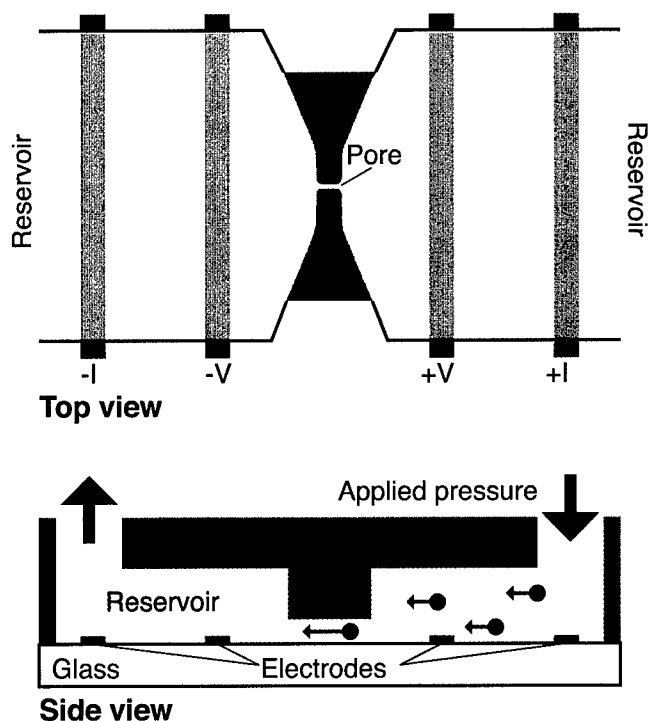
Top view

Side view

Fig. 1. Schematic side and top views of our device. We create the device by sealing a PDMS mold (containing two reservoirs connected by a pore) to a glass coverslip, and then filling it with solution. Pressure is used to drive the particles through the pore. The electrical current across the pore is measured at constant applied voltage by using a four-point technique, where the inner (outer) electrodes control the voltage (current). Incorporated into the top view is an optical image of an actual sealed device containing a 7-μm-long, 1-μm-wide pore.

voltage (0.2–0.5 V). Fig. 2 shows a typical measurement of the current: each downward pulse corresponds to a single colloid passing through the pore. Particle transit times are typically ≈200 μs when a pressure of ≈7 kPa (≈1 psi) is applied. Such transit times are long enough to establish a stable square pulse shape (see Fig. 2 *Inset*). We measure several hundred colloids in a given solution during a single experimental run, after which the device is either cleaned appropriately and reused or discarded. Custom-written software is used to extract both the height and width of each pulse in a trace. As described (24), the accuracy of the measurement is increased by using the measured width of each pulse to correct for the effect on the pulse height of a particle traveling off of the pore axis (25, 26).

Discussion

The goal of this work is to detect an increase in the magnitude of the pulses caused by the volume increase when ≈510-nm diameter streptavidin-coated latex colloids specifically bind to antibodies. The relative height of a pulse $\delta I/I$, where δI is the absolute pulse height and I is the baseline current value, depends on the relation of the diameter d of each colloid to the diameter D and length L of the pore (9, 15, 27–29). For the values of d (≈510 nm) and D (≈900 nm) used here, this relation is described by:

$$\left| \frac{\delta I}{I} \right| = \frac{D}{L} \left[\frac{\arcsin(d/D)}{\sqrt{1 - (d/D)^2}} - \frac{d}{D} \right]. \quad \text{[1]}$$

Using this equation, we can determine d for each streptavidin colloid measured if we know the dimensions of the pore. We directly measure L with an optical microscope. However, we
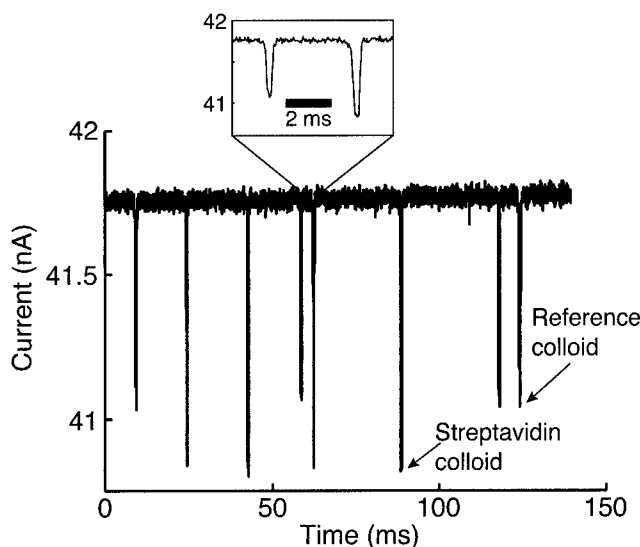

Fig. 2. A typical measurement of the current across a pore as different colloids pass through it. Each downward pulse corresponds to a single colloid transiting the pore. There is a clear difference in pulse magnitude as a result of the difference in size of the streptavidin colloids as compared with the reference colloids. This difference allows us to separate the pulses for pore calibration (see text). (*Inset*) An expanded view of two pulses. As shown, they are well resolved in time and consequently allow an unambiguous measurement of the pulse height. The data shown were taken with an applied voltage of 0.4 V and a pressure of ≈6.9 kPa.

cannot directly measure the pore's diameter D; instead, we perform a calibration by adding a reference colloid of known diameter (a 470-nm diameter sulfate-coated latex colloid) to each solution of streptavidin colloids. The absolute difference in diameter (470–510 nm) between the two types of colloids results in a clear difference in the pulse heights (see Fig. 2); consequently, we can determine easily which size colloid produced each pulse. We use the values of $\delta I/I$ arising from the reference colloids, along with the known values of L and d, to invert numerically Eq. **1** to thus determine the pore diameter D. Once this is accomplished, we use Eq. **1** once again to correlate the magnitude of each pulse to the diameter of the streptavidin colloid that produced it.

Fig. 3a shows a histogram comparing the distribution of measured colloid diameters obtained from two different solutions: one containing only the streptavidin and the reference colloids, and one containing both types of colloids and 0.1 mg/ml monoclonal mouse antistreptavidin antibody (with an affinity for streptavidin >10^{10}). As shown, there is a clear increase of 9 nm in the diameter of the streptavidin colloids in the solution containing the antibody (see also Fig. 3b). We attribute this increase to the volume added to the colloid on the specific binding to the antistreptavidin. Specificity is demonstrated by the much smaller increase in diameter (≈2.5 nm) when mixing the colloids with 0.1 mg/ml monoclonal isotype-matched irrelevant antibody (mouse anti-rabbit; see Fig. 3b). This smaller increase is a result of nonspecific binding of the irrelevant antibody to the colloids.

In Fig. 4 we show the measured change in colloid diameter as the concentration of the specific, high-affinity antibody (monoclonal antistreptavidin) is varied from 0.1 μg/ml to 100 μg/ml. As shown, the colloid diameter reaches its maximum value when the colloids are mixed with ≥5 μg/ml antibody. Using a Bradford protein assay (30), we determined the minimum saturating concentration of antibody for the colloid concentration in our experiment (1.2 × 10^9 particles per ml) to be 3.5 μg/ml, which is in good agreement with the results of our electronic pore-
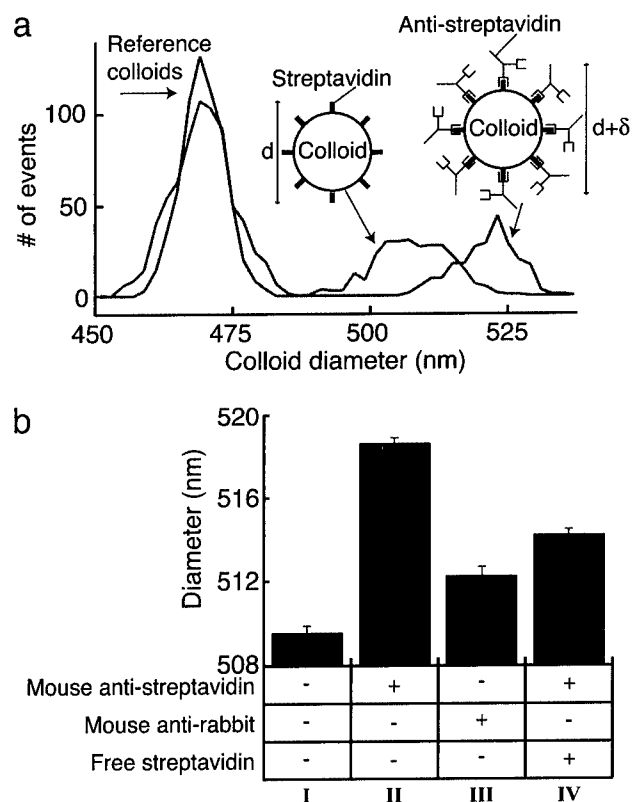
a

b

Fig. 3. (a) A histogram showing the distribution of colloid diameters measured from a solution that contains only the reference and streptavidin colloids (green line) and a solution that contains both types of colloids and 0.1 mg/ml monoclonal antistreptavidin antibody (red line). The specific binding of antistreptavidin to the streptavidin colloids produces a clear increase in the diameter of the colloids. (b) A summary of the measurements of the mean diameter of the streptavidin colloids when mixed in different solutions. A single experimental run consists of measuring several hundred colloids of each type in one solution; the plotted bars represent the mean diameter extracted from three to five such runs on the same solution, but using different devices. All solutions contained the streptavidin colloids and the reference colloids in a 0.5× PBS buffer (pH 7.3). The presence of additional components in each solution is indicated by a + in the column beneath the plotted bar. Column I shows the mean diameter measured without any protein added to the solution. A 9-nm increase in colloid diameter is seen in the presence of the specific antibody to streptavidin (0.1 mg/ml mouse antistreptavidin, column II); we attribute this to the volume added to the colloid caused by the specific binding of the antibody. The specificity of the probe is shown by the lack of a similar diameter increase in the presence of isotype-matched irrelevant antibody (0.1 mg/ml mouse anti-rabbit, column III); the small diameter increase in this solution can be attributed to nonspecific adhesion. We also perform an inhibition assay, where the specific binding of the antistreptavidin to the colloid is disrupted by the presence of 0.2 mg/ml free streptavidin (column IV) (the presence of free antigen is shown by the decrease in diameter compared with the antigen-free solution, column II). The error bars in all figures represent the uncertainty in determining the mean diameter based on one standard deviation of the measured distributions. The dominant source of error in our measurements is the intrinsic distribution in the streptavidin colloids' diameter, with smaller contributions from the spread in diameter of the reference colloids and the electrical noise in the current measurement.

based immunoassay. Furthermore, the manufacturer-quoted binding capacity of the colloids indicates that each colloid has ≈9,800 streptavidin molecules on its surface. If each colloid binds to an equivalent number of antibodies, the minimum saturating concentration for a solution containing 1.2×10^9 colloids/ml will be ≈3.0 μg/ml; again, this finding is in good agreement with our results. As shown in Fig. 4, the dynamic range of our assay corresponds to antibody concentrations from
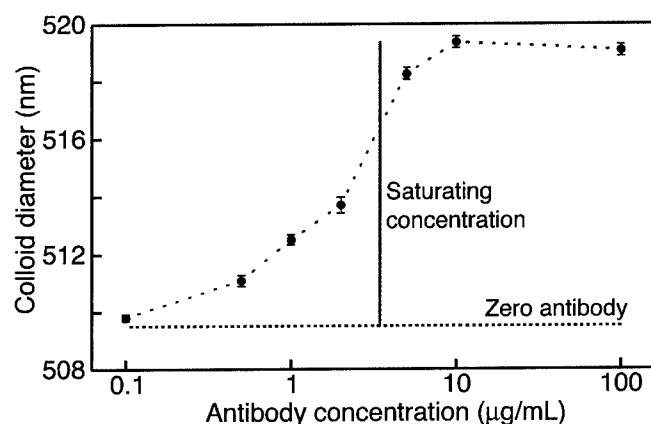

Fig. 4. Measurements of the mean colloid diameter when mixed in solutions of varying monoclonal mouse antistreptavidin concentrations. The vertical line marks the binding capacity of the colloids as determined by a Bradford protein assay. The diameter of the colloids in the absence of antibody is shown as the black dashed line.

0.5 μg/ml to the saturating concentration of ≈5 μg/ml. By decreasing the colloid concentration, we can decrease the binding capacity of the solution, thus decreasing the saturating concentration of antibody. In this manner, we can expect the range of sensitivity of the device to decrease to antibody concentrations as low as 10–50 ng/ml.

We use our technique's ability to detect successfully the specific binding of unlabeled antibodies to the colloids to perform an inhibition immunoassay. We measure a 4.5-nm increase (see column IV of Fig. 3b) in the diameter of the streptavidin colloids when mixed with 0.1 mg/ml antistreptavidin that had been preincubated with 0.2 mg/ml free streptavidin. This smaller increase (relative to the solution containing only antistreptavidin) indicates a decrease in the number of antibodies binding to each colloid. We primarily attribute this to the free streptavidin blocking the antibody binding sites. The measured diameter of the streptavidin-coated colloid therefore indicates the presence of free streptavidin in the solution. In general, this inhibition method can be extended to detect any antigen that can be immobilized on the colloid surface.

The 4.5-nm increase seen in column IV of Fig. 3b shows that some binding of antibody to the colloid does in fact occur. Based on the control measurement with an irrelevant antibody (column III of Fig. 3b), we attribute this increase to a combination of nonspecific binding of blocked antibodies and incomplete inhibition of the antibody by the free streptavidin. The possibility of nonspecific binding does decrease the dynamic range of the measurement. However, because of the very small uncertainty in the measured mean colloid diameter, the dynamic range necessary to determine the amount of ligand bound to the colloid is still quite large.

As a second demonstration of our technique's high sensitivity to the volume added by molecules bound to a streptavidin colloid, we perform an immunoassay (summarized in Fig. 5) with a sandwich configuration. Here, a primary antibody that is immobilized on the colloid surface binds to a free antigen, which in turn is bound to a secondary antibody. We immobilize the primary antibody by mixing streptavidin colloids with a biotinylated antibody (rabbit anti-*Streptococcus* group A) to thus create a colloid–antibody conjugate through the streptavidin–biotin bond. As shown in Fig. 5, the measured conjugated colloids are 514 nm in diameter, a 5-nm increase over the "bare" streptavidin colloids. Next, we mix the colloid–antibody conjugates with both the specific antigen to the primary antibody (extract from a culture of *Streptococcus* group A) and 0.1 mg/ml
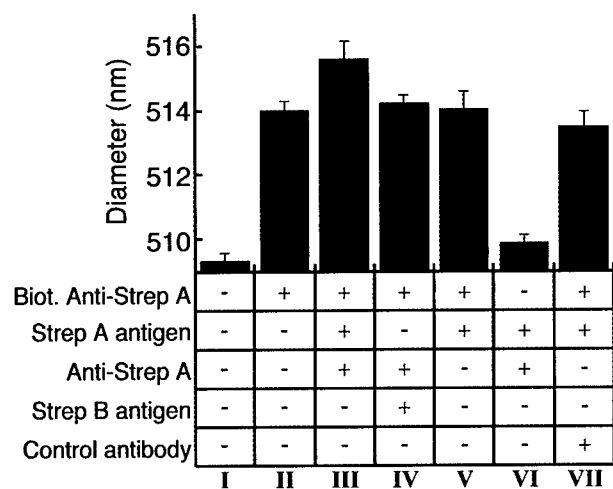
	I	II	III	IV	V	VI	VII
Biot. Anti-Strep A	-	+	+	+	+	-	+
Strep A antigen	-	-	+	-	+	+	+
Anti-Strep A	-	-	+	+	-	+	-
Strep B antigen	-	-	-	+	-	-	-
Control antibody	-	-	-	-	-	-	+

Fig. 5. Summary of the mean colloid diameters measured when forming an antibody–antigen–antibody "sandwich" on the colloid surface. All solutions contain the reference and streptavidin colloids in a 0.5× PBS buffer (pH 7.3), along with additional components as indicated by the + in the column below the plotted bar. Column I indicates the measured diameter of the bare streptavidin colloid. We measure a ≈5-nm increase (column II) in diameter after conjugating a biotinylated antibody (biotinylated anti-*Streptococcus* group A) to the streptavidin-coated colloids. A further increase of ≈1.6 nm is seen (column III) when adding both extract from a culture of *Streptococcus* group A and a secondary antibody specific to that antigen (unlabeled anti-*Streptococcus* group A); this increase indicates the formation of the sandwich on the colloid surface. The specificity of the configuration is shown by the lack of an increase in diameter when adding extract from a culture of *Streptococcus* group B (which is not bound by either antibody) in place of the group A extract (column IV), or an irrelevant antibody in place of the specific secondary antibody (column VII). When adding the specific antigen and secondary antibody to unconjugated colloids (column VI), we measure no significant diameter increase, indicating that nonspecific adhesion of antigen–secondary antibody complexes are not the cause of the diameter increase seen in column III. Finally, when adding the specific antigen alone to the conjugated colloids (column V), we see no increase in diameter, indicating that the diameter increase in column III is primarily caused by the binding of the secondary antibody.

secondary antibody (unlabeled rabbit anti-*Streptococcus* group A). Measurements of this solution show the colloids further increase in diameter by 1.6 nm. This 1.6-nm increase is not seen when the colloids are mixed with the antigen alone, indicating that the binding of the secondary antibody is the principal reason for the diameter increase. The specificity of this arrangement is demonstrated by the absence of a diameter increase in the control measurements we perform in which either the antigen or the secondary antibody is replaced by nonspecific counterparts (see Fig. 5).

It is intriguing that the measured 5-nm increase after attachment of the biotinylated antibody is less than the maximum 9-nm increase seen when using the antibody–antigen bond (Figs. 3 and 4) to attach antibody to the colloid. This surprising difference is most likely caused by the differing conformations of the antibody in each case; however, further work is needed to clarify this. Nonetheless, despite the smaller size increase, the ability of the device to perform the sandwich assay is still clearly demonstrated.

Although we have used an antibody/antigen reaction to demonstrate the power of our technique, we emphasize that its true strength is its generality: it does not rely on any functional properties of the free ligand. Thus, it can be applied to any ligand/receptor pair, provided the free ligand is large enough to produce a discernible change in the size of the colloid.

Future work on the device should focus on optimizing its sensitivity in terms of both ligand size (mass) and concentration. The sensitivity depends on four factors: the amount of ligand bound to each colloid, the intrinsic dispersion in colloid size, the colloid geometry, and the colloid concentration. First, increasing the number of binding sites will lead to more ligands bound per colloid, and consequently a larger change in size. For the colloids used here, the parking area for each binding site is ≈80 nm^2; although this is close to the steric limit for antibody molecules, the use of a smaller ligand would permit more binding sites per colloid. Second, the intrinsic spread in the sizes of the streptavidin colloids is the largest source of error in our measurement. The device's sensitivity would be enhanced by using a more monodisperse population of colloids (one with a coefficient of variation in diameter of <2%), or even a solution of highly monodisperse nanocrystals (31). Third, at constant binding density, the measured change in pulse height on binding to free ligand is proportional to the surface-to-volume ratio of the colloid. Thus, we could increase the sensitivity and dynamic range of the assay by using a smaller colloid. For example, we estimate that using a colloid 250 nm in diameter would increase the sensitivity of the assay by a factor of 4 in either ligand size or concentration. Thus, based on the data shown in Fig. 4, using a 250-nm colloid at the same particle concentration used in this article would make the assay sensitive to either 38-kDa ligand molecules at concentrations of 0.5 μg/ml or antibody concentrations near 0.1 μg/ml. We mention that an even more effective strategy to increase the surface-to-volume ratio would be to use a nonspherical or porous colloid (assuming the pore size is large enough to admit the free ligand) as the substrate for the immobilized receptor. Fourth, as previously mentioned, decreasing the concentration of colloids would further increase the sensitivity because it would decrease the minimum saturating concentration of free ligand. Overall, a combination of these four strategies should result in the increased sensitivity of our assay to ligand concentrations at or below 1 ng/ml.

In conclusion, we have demonstrated our ability to use an electronic measurement to detect the binding of unlabeled antibodies to the surface of latex colloids. This ability is generally applicable to determining rapidly and precisely the thickness of a layer of any kind of biological macromolecule bound to a colloid. Here, we specifically showed that our technique can be used to perform two widely used and important immunoassays (an inhibition assay and sandwich assay) in which either the antigen or antibody is immobilized on the colloid. In contrast to how these assays are performed today, ours requires no labeling of analytes, uses only submicroliter volumes of sample, and can be performed rapidly and inexpensively. For instance, we have compared our technique's ability (using a sandwich configuration) to detect the presence of *Streptoccocus* group A to that of a standard latex agglutination assay. We have found our method to be an order of magnitude more sensitive and more than four times as fast as the agglutination assay. Overall, our device can be used to detect many different kinds of analytes, because the colloids can be easily modified to have almost any specificity (through, for example, the biotin–streptavidin interaction used here). Furthermore, our technique can be extended to multianalyte detection not only by using several microparticles with different chemical sensitivities and different mean diameter but also by using devices consisting of arrays of pores (O.A.S., L. Dunkelberger, and L.L.S., unpublished work). Finally, in addition to a host of biosensing applications, this technique can be used as a diagnostic test of the surface chemistry of colloids.

APPLIED BIOLOGICAL

1. Luppa, P. B., Sokoll, L. J. & Chan, D. W. (2001) *Clin. Chim. Acta* **314,** 1–26.
2. Vo-Dinh, T. & Cullum, B. (2000) *Fresenius J. Anal. Chem.* **366,** 540–551.
3. Turner, A. P. (2000) *Science* **290,** 1315–1317.
4. Stefan, R. I., van Staden, J. F. & Aboul-Enein, H. Y. (2000) *Fresenius J. Anal. Chem.* **366,** 659–668.
5. Ngo, T. T. (2000) *Methods* **22,** 1–3.
6. Coulter, W. H. (1953) U.S. Patent No. 2,656,508.
7. Kubitschek, H. E. (1958) *Nature* **182,** 234–235.
8. Deblois, R. W. & Wesley, R. K. A. (1977) *J. Virol.* **23,** 227–233.
9. Deblois, R. W. & Bean, C. P. (1970) *Rev. Sci. Instrum.* **41,** 909–913.
10. Deblois, R. W., Bean, C. P. & Wesley, R. K. A. (1977) *J. Colloid Interface Sci.* **61,** 323–335.
11. Li, J., Stein, D., McMullan, C., Branton, D., Aziz, M. J. & Golovchenko, J. A. (2001) *Nature* **412,** 166–169.
12. Bayley, H. & Cremer, P. S. (2001) *Nature* **413,** 226–230.
13. Bezrukov, S. M., Vodyanoy, I. & Parsegian, V. A. (1994) *Nature* **370,** 279–281.
14. Gu, L. Q., Cheley, S. & Bayley, H. (2001) *Science* **291,** 636–640.
15. Saleh, O. A. & Sohn, L. L. (2001) *Rev. Sci. Instrum.* **72,** 4449–4451.
16. Sykulev, Y. K., Sherman, D. A., Cohen, R. J. & Eisen, H. N. (1992) *Proc. Natl. Acad. Sci. USA* **89,** 4703–4707.
17. von Schulthess, G. K., Benedek, G. B. & Deblois, R. W. (1983) *Macromolecules* **16,** 434–440.
18. von Schulthess, G. K., Benedek, G. B. & Deblois, R. W. (1980) *Macromolecules* **13,** 939–945.
19. von Schulthess, G. K., Deblois, R. W. & Benedek, G. B. (1978) *Biophys. J.* **21,** A115–A115.
20. Mullett, W. M., Lai, E. P. & Yeung, J. M. (2000) *Methods* **22,** 77–91.
21. Xia, Y. N. & Whitesides, G. M. (1998) *Angew. Chem. Int. Ed.* **37,** 551–575.
22. Whitesides, G. M. & Stroock, A. D. (2001) *Phys. Today* **54,** 42–48.
23. Chovan, T. & Guttman, A. (2002) *Trends Biotechnol.* **20,** 116–122.
24. Saleh, O. A. & Sohn, L. L. (2002) *Rev. Sci. Instrum.* **73,** 4396–4398.
25. Berge, L. I., Jossang, T. & Feder, J. (1990) *Meas. Sci. Technol.* **1,** 471–474.
26. Smythe, W. R. (1972) *Rev. Sci. Instrum.* **43,** 817–818.
27. Gregg, E. C. & Steidley, K. D. (1965) *Biophys. J.* **5,** 393–405.
28. Anderson, J. L. & Quinn, J. A. (1971) *Rev. Sci. Instrum.* **42,** 1257–1258.
29. Smythe, W. R. (1964) *Phys. Fluids* **7,** 633–638.
30. Bradford, M. M. (1976) *Anal. Biochem.* **72,** 248–254.
31. Bruchez, M., Jr., Moronne, M., Gin, P., Weiss, S. & Alivisatos, A. P. (1998) *Science* **281,** 2013–2016.

An Artificial Nanopore for Molecular Sensing

Omar A. Saleh and Lydia L. Sohn*

Department of Physics, Princeton University, Princeton, New Jersey 08544

Received February 5, 2002; Revised Manuscript Received November 15, 2002

ABSTRACT

We have used micromolding techniques to embed a nanoscale pore in PDMS. This novel design allows rapid and reproducible fabrication of pores, is extremely flexible, and can be modified both structurally and chemically for a variety of single-molecule detection applications. We demonstrate the capabilities of the device to sense electronically single DNA molecules.

Because ion-channel proteins are so finely tuned to respond to a single molecule, they have served as a model for developing nanopore devices for biomolecular sensing.[1] Two strategies for engineered nanopores—transmembrane protein pores suspended in lipid bilayers[2-5] and molecular-scaled holes in silicon nitride[6]—have achieved success in detecting single biological molecules; however, further development of these strategies is impeded by several technological barriers, including difficulties in creating an effective pore or array of pores and stabilizing it over a period of time. Here we report on a fundamentally different artificial nanopore that can be fabricated with great ease and control using micromolding techniques, is capable of sensing single molecules of unlabeled λ-phage DNA, and provides opportunities for diverse single-molecule detection applications.

Figure 1 shows one of our devices: a pore of length 3 μm and diameter 200 nm connecting two 5-μm-deep reservoirs. Well-established lithographic techniques are used to create a negative master of the pore and reservoirs, which is subsequently cast into a poly(dimethylsiloxane) (PDMS) slab. The master is created in two steps: first, electron-beam lithography is used to pattern a 200-nm-wide, 200-nm-thick polystyrene line on a silicon substrate, creating the negative of the pore. Next, photolithography is used to pattern an SU-8 photoresist on the substrate to form the negatives of the reservoirs. Both resists (polystyrene and SU-8) are exceptionally durable once cross linked, allowing us to reuse each master indefinitely. Following standard micromolding techniques,[7] we pour PDMS (Sylgard 184) over the master and cure it at 80 °C for at least 24 h. The PDMS slab is then removed from the master and sealed to a glass substrate that has previously defined platinum electrodes. The device is now complete and can be wet with the solution to be studied.

Molecules in the solution are driven through the pore either electrophoretically or by applying pressure to one of the
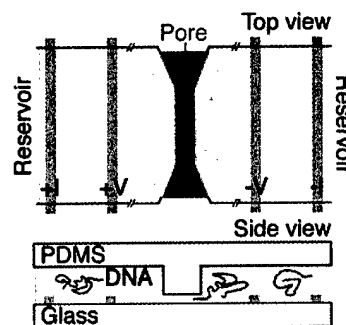

Figure 1. Schematic top and side views of our nanopore device, which consists of two 5-μm-deep reservoirs connected by a lateral pore of 3-μm length and 200-nm diameter; an optical image of an actual pore sealed to a glass coverslip is incorporated into the top view. Molecules in the reservoirs are electrophoretically drawn through the pore, partially blocking the flow of ions. The current through the pore is measured using a four-terminal technique, where the voltage and current controlling the platinum electrodes are as labeled.

reservoirs. When in the pore, the molecules partially block the flow of current, leading to transient increases in the pore's electrical resistance. Molecular sensing is accomplished by performing a four-point measurement of the electrical current through the pore using the platinum electrodes. The current is low-pass filtered below 0.3 ms in rise time and is sampled at 1 kHz using a voltmeter.

To demonstrate the sensing capabilities of our nanopore, we have measured solutions of 2.5 μg/mL λ-phage DNA in a 0.1 M KCl, 2 mM Tris (pH 8.4) buffer. Typical traces of measured current are shown in Figure 2. The striking downward peaks, of height 10−30 pA and width 2−10 ms, correspond to individual molecules of DNA passing through the pore. In contrast, such peaks are absent when measuring only buffer. We further note that peaks are present only when using pores with diameters of 300 nm or less.

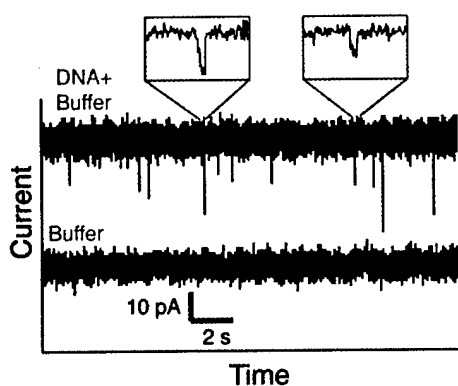* Corresponding author. E-mail: sohn@princeton.edu.

Figure 2. Typical traces of current vs time for solutions of buffer (lower trace) and buffer with λ-phage DNA molecules (upper trace) when 0.4 V is applied across the pore. The traces are offset for clarity; the total current in each case is $\sim$15 nA. Each downward spike in the lower trace represents a DNA molecule passing through the pore. The spikes are typically 2–10 ms in duration and are well resolved, as shown in the insets. The variations in peak height most likely correspond to the different conformation of each molecule.

Previous work on colloids[8,9] has shown that, for particles of diameter much smaller than that of the pore, the ratio of peak height to baseline current is approximately equal to the volume ratio of particle to pore: $\delta I/I \approx V_{particle}/V_{pore}$. We can estimate the volume of a single λ DNA molecule by approximating it as a cylinder with a 2-nm radius (which includes a 1-nm ionic, or Debye, layer) and a height equal to the contour length of the molecule ($\sim$16 μm). Given the known pore volume and a total current of $I = 15$ nA, we can expect a decrease in current of $\delta I \approx 30$ pA when a DNA molecule fully inhabits the pore. This estimate agrees well with the upper range of measured peak heights. Further corroboration for this model comes from the fact that no peaks are observed when using larger pores (pores >300 nm in diameter). When a molecule inhabits a pore with a diameter >300 nm, the expected response in current is less than 40% of that for a 200-nm-diameter pore. Therefore, at 15 nA of total current, the maximum peak heights for a λ DNA molecule will be less than 12 pA, a value not well resolvable above the noise. Our results suggest that the measured variation in δI is most likely due to differences in molecular conformation: maximum peak heights arise when an entire molecule inhabits the pore, whereas smaller peak heights occur when only a portion of a molecule resides within the pore. Future experiments will focus on controlling

the conformation of each molecule to relate the measured peak height to the length of each DNA molecule. Thus, our nanopore device may provide a simple and quick method for the coarse sizing of large DNA molecules.

The results described here represent the first step toward a host of single-molecule sensing applications. By relying on common microfabrication techniques, we can easily create arrays of pores for the simultaneous measurement of many different molecules.[10] Decreasing the pore size will allow us to detect and size smaller molecules such as proteins or viruses. The minimum achievable pore diameter for the PDMS used here (Sylgard 184) is $\sim$150 nm, but recent work has shown that other PDMS formulations can maintain features as small as 80 nm.[11] Finally, we can add chemical specificity in two ways: First, by covalently attaching molecules of interest to the pore wall, we expect to see changes in the transit times of molecules in solution that interact with the immobilized molecules. Second, we can measure changes in the diameter of chemically functionalized colloids upon binding of molecules in the solution, as we have already done using micrometer-scale colloids and pores.[12] The ease and reproducibility of micromolding and the simplicity of our device greatly enhance the capabilities of artificial nanopores for molecular sensing.

References

(1) Bayley, H.; Cremer, P. S. *Nature (London)* **2001**, *413*, 226–230.
(2) Bezrukov, S. M.; Kasianowicz, J. J. *Phys. Rev. Lett.* **1993**, *70*, 2352–2355.
(3) Bezrukov, S. M.; Vodyanoy, I.; Parsegian, V. A. *Nature (London)* **1994**, *370*, 279–281.
(4) Braha, O.; Walker, B.; Cheley, S.; Kasianowicz, J. J.; Song, L.; Gouaux, J. E.; Bayley, H. *Chem. Biol.* **1997**, *4*, 497–505.
(5) Kasianowicz, J. J.; Brandin, E.; Branton, D.; Deamer, D. W. *Proc. Natl. Acad. Sci. U.S.A.* **1996**, *93*, 13770–13773.
(6) Li, J.; Stein, D.; McMullan, C.; Branton, D.; Aziz, M. J.; Golovchenko, J. A. *Nature (London)* **2001**, *412*, 166–169.
(7) Xia, Y. N.; Whitesides, G. M. *Angew. Chem., Int. Ed.* **1998**, *37*, 551–575.
(8) Deblois, R. W.; Bean, C. P. *Rev. Sci. Instrum.* **1970**, *41*, 909–913.
(9) Saleh, O. A.; Sohn, L. L. *Rev. Sci. Instrum.* **2001**, *72*, 4449–4451.
(10) Saleh, O. A.; Sohn, L. L.; Dunkleberger, L. N. I. To be submitted for publication.
(11) Schmid, H.; Michel, B. *Macromolecules* **2000**, *33*, 3042–3049.
(12) Saleh, O. A.; Sohn, L. L. Submitted for publication.

NL0255202

Correcting off-axis effects in an on-chip resistive-pulse analyzer

O. A. Saleh and L. L. Sohn[a]

Department of Physics, Princeton University, Princeton, New Jersey 08544

A resistive-pulse analyzer is a device that utilizes measurements of the electrical resistance of a solution-filled pore to determine the size of particles that pass through the pore. The relation between particle size and changes in the pore's resistance is complicated by particles that travel off the central axis of the pore. Here, we present data taken using a microfabricated pore and latex colloids that illustrates the effects of off-axis particles, and propose an algorithm for removing those effects from the data. We show that the ability to remove off-axis effects increases the precision of devices that transport particles through the pore with a pressure-driven flow relative to those that use electrophoretic flow. © *2002 American Institute of Physics.* [DOI: 10.1063/1.1519932]

Resistive-pulse analysis is a method for measuring the size of particles in a solution: A particle passing through a solution-filled pore displaces conducting fluid which in turn causes a transient increase in the electrical resistance of the pore that is quantitatively related to the size of the particle. This technique has been used to measure the size and concentration of a variety of particles, such as cells,[1] viruses,[2] and colloids.[3] In those cases, the pore was made using relatively complicated methods, such as etching the tracks of radioactive particles after they have passed through a material.

Recently,[4] we utilized relatively simple microfabrication techniques to develop the first chip-based microfluidic device capable of sizing submicron particles in a solution through the resistive pulse technique. In that initial work, we drove the particles through the pore electrophoretically, thus requiring the particles to carry a relatively high electrostatic charge for effective electric-field-driven motion. Motivated by the desire to measure particles that are not highly charged, such as viruses or protein-coated colloids, we have developed a second version of the device that utilizes hydrostatic pressure to drive the particles through the pore.

The analysis of the pulses produced while utilizing a pressure-driven flow is complicated by the effects of particles that travel off the central axis of the pore. Relative to particles of identical size that travel on axis, off-axis particles take longer to transit the pore (causing wider pulses) and produce larger electrical resistance changes. The former effect, which we refer to as the hydrodynamic off-axis effect, is simply due to the parabolic distribution of fluid velocity within the pore. The latter effect, which we refer to as the electrical off-axis effect, occurs because off-axis particles enhance the nonuniformity in the distribution of electrical current density and, consequently, further increase the electrical resistance.[5] In this Note, we present two main results. First, we show how off-axis particles affect data taken on populations of colloidal particles and propose a method to remove

these effects. Second, we point out that a device utilizing a pressure-driven flow will have an increased resolution over one using an electrophoretic flow, since the algorithm we have developed to remove off-axis effects can only be performed for a pressure-driven flow. As we will demonstrate, both results should increase the precision of future applications of the resistive-pulse technique.

To quantitatively describe our data, we follow the work of Berge *et al.*,[6] who formulated phenomenological equations to describe the two aforementioned off-axis effects. For the hydrodynamic effect, they found that previous experimental data[7] on the time τ for a particle to pass through the pore are well described by

$$\tau = \frac{\tau_0}{(1-x^2)(c_1 - c_2 x^5)}, \tag{1}$$

where $\tau_0 = 16\eta(L/D)^2/\Delta P$ is the on-axis transit time for an infinitely small particle, η is the fluid viscosity, L is the pore length, D is the pore diameter, ΔP is the pressure drop across the pore, $x = 2b/D$ is the fractional radial position for a particle centered a distance b off of the pore axis, $c_1 = 1 - (2/3)(d/D)^2$, $c_2 = 23.36(1-c_1)$, and d is the particle diameter (see Fig. 1). Berge *et al.*[6] then utilized Eq. (1) to empirically describe the variation in the change in electrical resistance ΔR with an off-axis coordinate x as

$$\Delta R = \Delta R_0 \left[1 + \alpha \left(\frac{xd}{D} \right)^3 \right], \tag{2}$$

where $\Delta R_0(d,D,L)$ is the change in resistance for the on-axis particle (see Ref. 1 for its functional form) and α is a constant whose value varies between 4.2 and 7.5.

In Fig. 2, we plot the values we measured of the normalized change in electrical resistance $\Delta R/R$ versus τ for pulses produced by two populations of latex colloids: one population with a mean diameter of 470 nm, and one with a mean diameter of 514 nm. The data were taken using a pore that is 9.4 μm in length and 1.16 μm in diameter. For both types of colloids, there is a clear positive and nearly linear correlation between $\Delta R/R$ and τ as qualitatively expected from Eqs. (1) and (2). One interpretation of this positive correlation is that

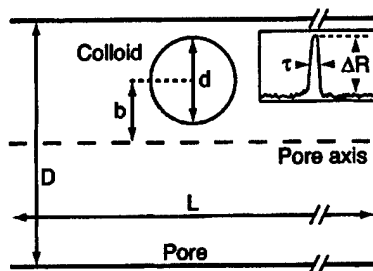[a]Author to whom correspondence should be addressed; electronic mail: sohn@princeton.edu

FIG. 1. Schematic of the measurement geometry for a pore of diameter D and length L containing a colloid of diameter d that travels a distance b off the pore axis. Inset: Typical trace of the measured resistance vs time showing the passage of a single colloid that produces a resistance pulse of width τ and height ΔR.

FIG. 3. Histogram of the normalized pulse heights ($\Delta R/R$) measured for a solution containing four different sizes of latex colloids (of diameters 370, 460, 560, and 640 nm as labeled); each peak corresponds to the colloids of a given size. The dotted line represents the raw data while the solid line shows the same data after correcting for the effects of off-axis particles, as described by Eq. (3). The distribution of measured pulse heights for each type of colloid is both sharpened and more symmetric after applying the correction. For example, the application of the adjustment caused a decrease in the coefficient of variation of the pulses measured from the 560 nm colloids from 7.1% to 3.5%.

it is due to deviations in the size of individual colloids within each population, since it is clear that relatively larger colloids will both move slower and produce larger pulse amplitudes. The 470 nm diameter colloid population shown in the lower portion of the data plotted in Fig. 2 has a standard deviation of 12 nm as measured by the manufacturer. Equation (1) predicts that the expected variation in τ of on-axis particles, due solely to differences in particle size within the population, will be $\sim 2\%$. As seen in Fig. 2, the measured values for τ vary by much more than that ($\sim 80\%$). We thus conclude that the measured variations in τ can be attributed almost entirely to off-axis effects and not to differences in particle size.

Given particle and pore dimensions, we can use Eqs. (1) and (2) to find the predicted dependence of ΔR on τ due to the off-axis effects. In Fig. 2, we plot this result and compare it to the measured data. For both types of colloids, we find good agreement between the predicted dependence and the measurements when $\alpha = 6$ in Eq. (2); this value of α falls well within the range found by Berge et al.[6] The nearly linear measured correlation between ΔR and τ is then explained by the fact that variations in ΔR (caused by both electrical noise and the intrinsic size distribution of the colloid population) obscure the slight nonlinearity in the predicted dependence. Based on this, we propose that off-axis effects can be
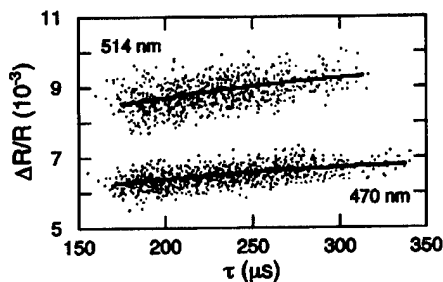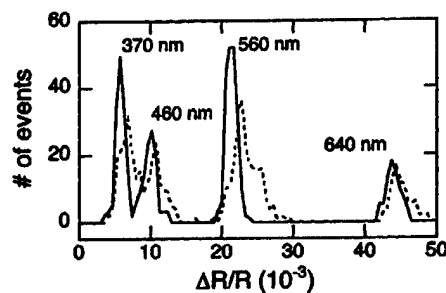
effectively removed in the data analysis of a given population by first fitting a line $f(\tau)$ to the plot of ΔR versus τ, and then calculating an adjusted value ΔR_{adj} for each event of height ΔR and width τ:

$$\Delta R_{adj} = \Delta R - [f(\tau) - f(\tau_{min})],\qquad(3)$$

where $\tau_{min} = \tau_0/c_1$ is the minimum transit time measured. We thus use Eq. (3) as an algorithm to calculate the pulse height each colloid would have caused had it traveled on the central axis of the pore.

To illustrate the increase in resolution that results from employing Eq. (3), we have measured a polydisperse solution containing four different sizes of latex colloids (of diameters 370 nm, 460 nm, 560 nm, and 640 nm). In Fig. 3, we plot the distribution of measured ΔR values both before and after applying Eq. (3). As shown, the correction clearly sharpens the distribution for each type of colloid. For example, the coefficient of variation (standard deviation divided by mean) for pulses produced by 560 nm diameter colloids is reduced from 7.1% to 3.5%.

Previously,[4] we utilized an electrophoretic driving force and found relatively little correlation between the measured pulse heights and widths. In that data, we measured linear correlation coefficients R ranging from 0.1 and 0.2 between the pulse heights and widths; this is in contrast to typical values of $R \sim 0.5$ for data obtained using a pressure-driven flow. Since we expect that the electrical off-axis effect must have been present in the electrophoretically driven data, we conclude that the electrophoretic velocity of the measured colloids does not vary significantly with the off-axis coordinate. This agrees with the fact that, in the absence of a colloid, the electric field across the pore is constant. It is possible that an off-axis effect on the velocity of a particle subjected to only an electrophoretic force would be caused by either inhomogenieties in the electric field due to the presence of the particle, or hydrodynamic interactions between the particle and pore wall. We can only conclude that these

FIG. 2. Comparison of measured normalized pulse heights ($\Delta R/R$) and pulse widths (τ) and the predictions of Eqs. (1) and (2). Each point represents the measured pulse height vs pulse width for the passage of a 470 nm diameter latex colloid (lower group of points) or a 514 nm diameter latex colloid (upper group of points) through a pore of length 9.4 μm and diameter 1.16 μm. For each type of colloid, the correlation between the measured heights and widths of the pulses is a result of the effect of colloids that travel off the pore axis. The measured data agree well with the predictions of Eqs. (1) and (2) for each colloid size, shown here as the solid lines.

O. A. Saleh and L. L. Sohn

possible effects are insignificant compared to the noise in our measurement.

The absence of an observable hydrodynamic off-axis effect while using an electrophoretic flow means that we are unable to apply an algorithm similar to Eq. (3) to remove the electrical off-axis effect for electrophoretic data. Distributions of pulse heights of a given colloid population measured using an electrophoretic driving force are, therefore, reduced in accuracy since they contain an intractable systematic source of error: the electrical off-axis effect. Devices using a pressure driven flow, where we are able to apply the correction described in Eq. (3), are thus more accurate than those that use electrophoretic flow.

[1] W. H. Coulter, U.S. Patent No. 2,656,508 (20 October 1953); H. E. Kubitschek, Nature (London) **182**, 234 (1958).

[2] R. W. Deblois and R. K. A. Wesley, J. Virol. **23**, 227 (1977).

[3] R. W. Deblois and C. P. Bean, Rev. Sci. Instrum. **41**, 909 (1970); R. W. Deblois, C. P. Bean, and R. K. A. Wesley, J. Colloid Interface Sci. **61**, 323 (1977).

[4] O. A. Saleh and L. L. Sohn, Rev. Sci. Instrum. **72**, 4449 (2001).

[5] J. C. Maxwell, *A Treatise on Electricity and Magnetism*, 3rd ed. (Clarendon, Oxford, 1904).

[6] L. I. Berge, T. Jossang, and J. Feder, Meas. Sci. Technol. **1**, 471 (1990).

[7] H. L. Goldsmith and S. G. Mason, J. Colloid Sci. **17**, 448 (1962).

Quantitative sensing of nanoscale colloids using a microchip Coulter counter

O. A. Saleh and L. L. Sohn[a)]

Department of Physics, Princeton University, Princeton, New Jersey 08544

We have fabricated a microchip Coulter counter on a quartz substrate, and have used it to detect individual nanoscale colloidal particles with a sensitivity proportional to each particle's size. We demonstrate the ability of this device to sense colloids as small as 87 nm diameter, and to distinguish between colloids whose diameters differ by less than 10%. Further reductions in the pore size, easily done with current nanofabrication techniques, make our device applicable to measuring biological macromolecules, such as DNA and proteins. © *2001 American Institute of Physics.*
[DOI: 10.1063/1.1419224]

I. INTRODUCTION

Quantitative measurements of the size and concentration of nanoscale particles are critical for studies of colloidal and macromolecular solutions. Traditionally, this is accomplished through ultracentrifugation, chromatography, gel electrophoresis,[1] or dynamic light scattering.[2] Here we discuss an alternative method based on the Coulter technique of particle sensing.[3] Coulter counters typically consist of two reservoirs of particle-laden solution separated by a membrane and connected by a single pore through that membrane. By monitoring changes in the electrical current through the pore as individual particles pass from one reservoir to another, a Coulter counter can measure the size of particles whose dimensions are on the order of the pore dimensions. While this method has long been used to characterize cells several microns in diameter,[4,5] its relative simplicity has led to many efforts to employ it to detect nanoscale particles,[6–9] including viruses.[10]

In this article, we present the first working realization of a Coulter counter on a microchip. Our device, fabricated on top of a quartz substrate using standard microfabrication techniques, utilizes a four-point measurement of the current through the pore. We are able to control precisely the pore dimensions, which we can easily measure using optical and atomic force microscopies. Knowing the exact pore dimensions allows us to predict quantitatively the response of the device to various sized particles. We have fabricated pores with lateral dimensions between 400 nm and 1 μm, and used them to detect latex colloidal particles as small as 87 nm in diameter. Furthermore, we demonstrate the ability of the device to detect ~500 nm diam colloids with a resolution of ±10 nm. The device has numerous applications in sizing and separating nanoscale particles in solution, and is easily integrated with other on-chip analysis systems.

[a)]Author to whom correspondence should be addressed; electronic mail: sohn@princeton.edu

II. EXPERIMENT

Our device, shown in Fig. 1(a), is fabricated in multiple stages. Each stage consists of lithographic pattern generation, followed by pattern transfer onto a quartz substrate using either reactive ion etching (RIE) or metal deposition and liftoff. The first stage is the fabrication of the pore. A line is patterned on the substrate using either photolithography (PL) for linewidths ≥ 1 μm, or electron-beam lithography (EBL) for linewidths between 100 and 500 nm, and then etched into the quartz using a CHF_3 RIE. The substrate subsequently undergoes a second stage of PL and RIE to define two reservoirs that are 3.5 μm deep, separated by 10 μm, and connected to each other by the previously defined channel [see Fig. 1(a)]. The length of the pore is defined in this second stage by the separation between the two reservoirs. The final stage consists of patterning four electrodes across the reservoirs, followed by two depositions of 50/250 Å Ti/Pt in an
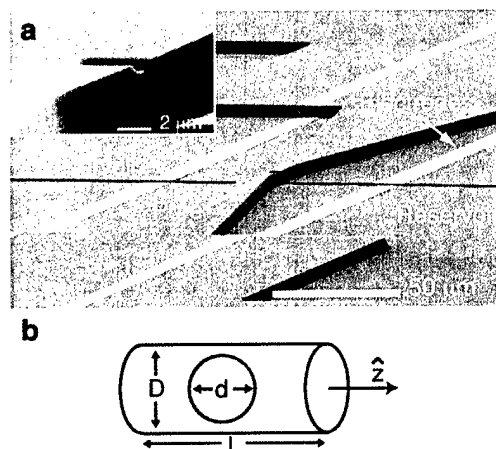

FIG. 1. (a) Scanning electron micrograph of our microchip Coulter counter. The 3.5 μm deep reservoirs and the inner Ti/Pt electrodes, which control the voltage applied to the pore but pass no current, are only partially shown. The outer electrodes, which inject current into the solution, are not visible in this image. The inset shows a magnified view of this device's pore, which has dimensions $5.1 \times 1.5 \times 1.0$ μm^3. (b) A schematic diagram of a spherical particle of diameter d in a pore of diameter D and length L.
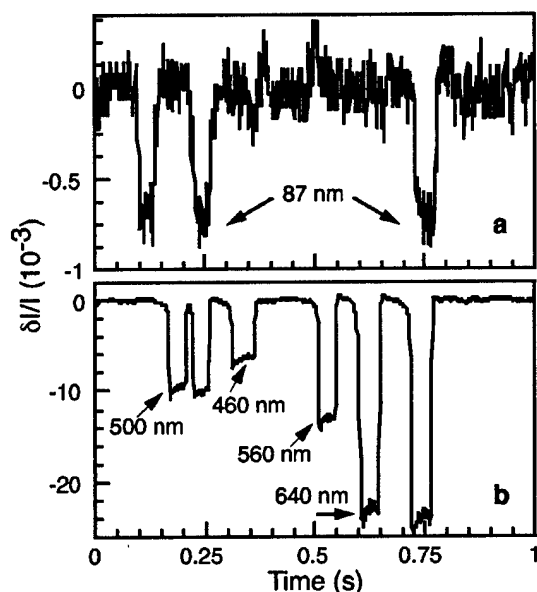
FIG. 2. Relative changes in baseline current $\delta I/I$ vs time for (a) a monodisperse solution of 87 nm diam latex colloids measured with an EBL-defined pore of length 8.3 μm and cross section 0.16 μm^2, and (b) a polydisperse solution of latex colloids with diameters 460, 500, 560, and 640 nm measured with a PL-defined pore of length 9.5 μm and cross section 1.2 μm^2. Each downward current pulse represents an individual particle entering the pore (Ref. 14). The four distinct pulse heights in (b) correspond as labeled to the four different colloid diameters.

electron-beam evaporator with the sample positioned $\pm 45°$ from normal to the flux of metal to ensure that the electrodes are continuous down both walls of the reservoirs.

The device is sealed on top of with a silicone-coated (Sylgard 184, Dow Corning Corp.) glass coverslip before each measurement. Prior to sealing, both the silicone and the substrate are oxidized in a dc plasma to ensure the hydrophilicity[11] of the reservoir and pore and to strengthen the seal[12] to the quartz substrate. After each measurement, the coverslip is removed and discarded, and the substrate is cleaned by chemical and ultrasonic methods.[13] Thus, each device can be reused many times.

We have measured solutions of negatively charged (carboxyl-coated) latex colloids (Interfacial Dynamics, Inc.) whose diameters range from 87 to 640 nm. All colloids were suspended in a solution of 5× concentrated Tris–Borate–EDTA (TBE) buffer with a resistivity of 390 Ω cm and pH 8.2. To reduce adhesion of the colloids to the reservoir and pore walls, we added 0.05% volume to volume (v/v) of the surfactant Tween 20 to every solution. The colloidal suspensions were diluted significantly from stock concentrations to avoid jamming of colloids in the pore; typical final concentrations were $\sim 10^8$ particles/ml. The pore and reservoirs were filled with solution via capillary action.

III. THEORY

The sensitivity of a Coulter counter relies upon the relative sizes of the pore and the particle to be measured. The resistance of a pore R_p increases by δR_p when a particle
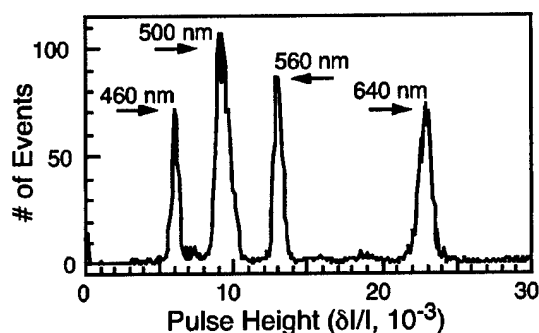

FIG. 3. A histogram of pulse heights resulting from measuring the polydisperse solution shown in Fig. 2(b). The resolution for this particular device is ± 10 nm in diameter for the particles measured.

enters since the particle displaces conducting fluid. δR_p can be estimated[5] for a pore aligned along the z axis [see Fig. 1(b)] by

$$\delta R_p = \rho \int \frac{dz}{A(z)} - R_p,\qquad(1)$$

where $A(z)$ represents the successive cross sections of the pore containing a particle, and ρ is the resistivity of the solution. For a spherical particle of diameter d in a pore of diameter D and length L, the relative change in resistance is

$$\frac{\delta R_p}{R_p} = \frac{D}{L}\left[\frac{\arcsin(d/D)}{(1-(d/D)^2)^{1/2}} - \frac{d}{D}\right].\qquad(2)$$

Equations (1) and (2) assume that the current density is uniform across the pore, and thus is not applicable for cases where the cross section $A(z)$ varies quickly, i.e., when $d \ll D$. For that particular case, Deblois and Bean[6] formulated an equation for δR_p based on an approximate solution to the Laplace equation:

$$\frac{\delta R_p}{R_p} = \frac{d^3}{LD^2}\left[\frac{D^2}{2L^2} + \frac{1}{\sqrt{1+(D/L)^2}}\right]F\left(\frac{d^3}{D^3}\right),\qquad(3)$$

where $F(d^3/D^3)$ is a numerical factor that accounts for the bulging of the electric field lines into the pore wall. When employing Eq. (3) to predict resistance changes, we find an effective value for D by equating the cross sectional area of our square pore with that of a circular pore.

If R_p is the dominant resistance of the measurement circuit, then relative changes in the current I are equal in magnitude to the relative changes in the resistance $|\delta I/I|$ $= |\delta R_p/R_p|$ and Eqs. (2) and (3) can both be directly compared to measured current changes.

This comparison is disallowed if R_p is similar in magnitude to other series resistances, such as the electrode/fluid interfacial resistance $R_{e/f}$ or the resistance R_u of the reservoir fluid between the inner electrodes and the pore. We completely remove $R_{e/f}$ from the electrical circuit by performing a four-point measurement of the current [see Fig. 1(a)]. We minimize R_u by placing the inner electrodes close to the pore (50 μm away on either side), and by designing the reservoir with a cross section much larger than that of the pore. For a pore of dimensions 10.5 μm by 1.04 μm^2, we measured $R_p = 36$ MΩ, in good agreement with the 39 MΩ value pre-
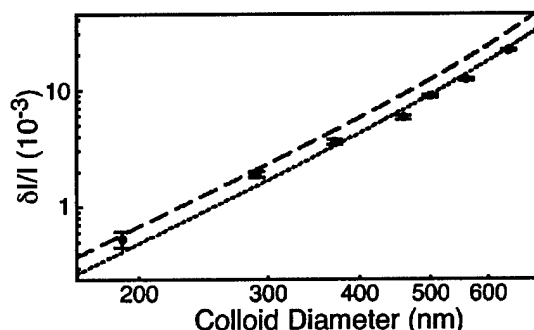
FIG. 4. Comparison of measured $\delta I/I$ values (circles) to those predicted by Eq. (2) (dotted line) and Eq. (3) (dashed line). The measured data were taken over several runs on a single PL-defined pore of length 10.6 μm and cross section 1.04 μm². Error bars for the larger colloid sizes are obscured by the size of the plotted point. As the colloid diameter increases, there is a transition from agreement with Eq. (3) to Eq. (2). This reflects the fact that the derivation of Eq. (3) assumes the colloid diameter d is much less than the pore diameter D; conversely Eq. (2) relies on an assumption that holds only as d approaches D, and breaks down for smaller colloids.

dicted by the pore geometry and the solution resistivity. This confirms that we have removed R_u and R_{eff} from the circuit.

IV. RESULTS AND DISCUSSION

Figure 2 shows representative data resulting from measuring a monodisperse solution of colloids 87 nm in diameter with an EBL-defined pore [Fig. 2(a)], and from measuring a polydisperse solution containing colloids of diameters 460, 500, 560, and 640 nm with a PL-defined pore [Fig. 2(b)]. Each downward current pulse in Fig. 2 corresponds to a single colloid passing through the pore.[14] For the data shown, 0.4 V was applied to the pore. In other runs, the applied voltage was varied between 0.1 and 1 V to test the electrophoretic response of the colloids. We found that the width of the downward current pulses varied approximately as the inverse of the applied voltage, as is expected for simple electrophoretic motion

Figure 3 shows a histogram of ~3000 events measured for the polydisperse solution. The histogram shows a very clear separation between the pore's response to the differently sized colloids. The peak widths in Fig. 3 represent the resolution of this device, which we find to be ±10 nm in diameter for the measured colloids. This precision approaches the intrinsic variations in colloid diameter of 2%–

4%, as given by the manufacturer. In this run, the maximum throughput was 3 colloids/s, a rate easily achievable for all of our samples. Event rates are limited by the low concentrations needed to avoid jamming.

We used a device whose pore size was 10.5 μm by 1.05 μm² to measure colloids ranging from 190 to 640 nm in diameter. Figure 4 shows a comparison between the measured mean pulse heights and those predicted by Eqs. (2) and (3). As shown, there is excellent agreement between the measured and calculated values, with the measured error insignificant compared to the range of pulse heights. In addition, the measurements more closely follow Eq. (3) for small d and Eq. (2) for larger d, as was anticipated in the derivation of those equations.

ACKNOWLEDGMENTS

[1] B. Alberts, D. Bray, J. Lewis, M. Raff, K. Roberts, and J. D. Watson, *Molecular Biology of the Cell* (Garland, New York, 1994).
[2] W. B. Russel, D. A. Saville, and W. R. Schowalter, *Colloidal Dispersions* (Cambridge University Press, New York, 1989).
[3] W. H. Coulter, U. S. Patent No. 2,656,508 (20 Oct. 1953).
[4] H. E. Kubitschek, Nature (London) **182**, 234 (1958).
[5] E. C. Gregg and K. D. Steidley, Biophys. J. **5**, 393 (1965).
[6] R. W. Deblois and C. P. Bean, Rev. Sci. Instrum. **41**, 909 (1970).
[7] M. Koch, A. G. R. Evans, and A. Brunnschweiler, J. Micromech. Microeng. **9**, 159 (1999).
[8] L. Sun and R. M. Crooks, Langmuir **15**, 738 (1999).
[9] Y. Kobayashi and C. R. Martin, J. Electroanal. Chem. **431**, 29 (1997).
[10] R. W. Deblois, C. P. Bean, and R. K. A. Wesley, J. Colloid Interface Sci. **61**, 323 (1977).
[11] D. W. Fakes, M. C. Davies, A. Browns, and J. M. Newton, Surf. Interface Anal. **13**, 233 (1988).
[12] M. K. Chaudhury and G. W. Whitesides, Langmuir **7**, 1013 (1991).
[13] After removing the coverslip, the substrate is soaked in Amtex CCR (Amtex Chemical Co.) for several hours to remove silicone residue, then rinsed in de-ionized water. Remnant colloids are removed by briefly sonicating the substrate in toluene, then rinsing in methanol. Finally, all remaining particulate residue is removed using the RCA SC1 cleaning procedure, which consists of a heated bath of 5:1:1 $H_2O:NH_4OH:H_2O_2$. The substrate is then ready to be resealed.
[14] We have seen events that clearly correspond to two colloids simultaneously inhabiting the pore. Such two-particle events are easily differentiated from one-particle events by their anomalous pulse heights and widths.

Dielectric spectroscopy for bioanalysis: From 40 Hz to 26.5 GHz in a microfabricated wave guide

G. R. Facer[a)]
Department of Physics, Princeton University, Princeton, New Jersey 08544

D. A. Notterman
Department of Molecular Biology, Princeton University, Princeton, New Jersey 08544

L. L. Sohn
Department of Physics, Princeton University, Princeton, New Jersey 08544

We report developing coplanar waveguide devices which can perform dielectric spectroscopy on biological samples within a microfluidic channel or well. Since coupling to the fluid sample is capacitive, no surface functionalization or chemical sample preparation are required. Data on cell suspensions and solutions of proteins and nucleic acids spanning the frequency range from 40 Hz to 26.5 GHz are presented. Low-frequency data are well explained using a simple dispersion model. At microwave frequencies, the devices yield reproducible and distinguishable spectral responses for hemoglobin solution and live *E. coli.* © *2001 American Institute of Physics.*
[DOI: 10.1063/1.1347020]

Rapid characterization of biological specimens is increasingly important in research and clinical applications. While current optical and chemical detection techniques[1-3] can effectively analyze biological systems, a number of disadvantages restrict their versatility. As examples: most samples must be chemically altered prior to analysis, and photobleaching can place a time limit on optically probing fluorophore-tagged samples. Purely electronic techniques provide solutions to many such problems, as they can probe a sample and its chemical environment directly over a range of time scales, without requiring chemical modifications.[4,5] One example of electronic detection is dielectric spectroscopy:[6-10] examining permittivity as a function of frequency. This direct, nondestructive, and sensitive technique can probe a system at various length scales, from centimeters to microns, with sample volumes as small as picoliters.[11,12]

In this letter, we describe coplanar waveguide (CPW) devices for performing dielectric spectroscopy on samples confined to a microfluidic channel or well across nearly 9 orders of magnitude in frequency, from 40 Hz to 26.5 GHz. Because coupling to the sample is capacitive, our CPWs allow measurements from dc to microwave frequencies, *without* the need for surface functionalization or chemical binding.[12] A very wide range of species can therefore be analyzed rapidly and directly. The planar geometry of our devices allows for straightforward integration with microfluidic systems.[5,13,14] Below, we discuss the fabrication of the CPW devices, and the low-frequency to microwave spectra which we have obtained for biomolecular solutions and cell suspensions.

Permittivity measurements across a range of frequencies ("dielectric spectra") provide information about the species present and their chemical environment. Features in dielectric spectra—all relating to polarization relaxations[7,15-18]—

are generally classified as α-, β-, or γ-dispersions. α-dispersion is the permittivity enhancement by rearrangements of small ions, including screening at the fluid interface. β-dispersion arises from distortions of cellular membranes and macromolecules. γ-dispersion is due to rotations and deformations of small, polar molecules or groups (frequently the solvent itself). Access to a broad frequency range is imperative with biological samples, due to their chemical diversity:[19,20] in solutions with total ionic strengths $\gtrsim 0.1$ M, α-dispersion extends up to $\gtrsim 1$ GHz, while β-dispersions extend from $\lesssim 1$ kHz[21] up to the relaxational modes of macromolecules in the infrared (THz) and beyond.

Dielectric spectra for α-, β-, and γ-dispersions have a common form:[15,22] at low frequencies, the polarization is able to closely follow the applied electric field (relative permittivity $\epsilon = \epsilon_{LF}$), while at high frequencies applied excitations oscillate too fast for the charges to respond ($\epsilon = \epsilon_{HF}$). Generally, $\epsilon_{LF} \gg \epsilon_{HF}$.

A schematic diagram of our CPW devices is shown in Fig. 1. They are symmetric metal transmission lines comprised of a 40 μm wide central strip bordered by two grounded 380 μm wide conductors. Each metal region is an evaporated Ti/Au (50 Å/500 Å) base topped with an elec-
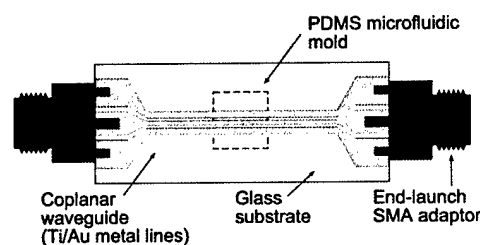

FIG. 1. CPW device, showing the Ti/Au wave guide (not to scale) and microfluidic sample containment. Across the central portion, the inner line width is 40 μm, outer line widths 380 μm, and the inner–outer separation is 7 μm. Total substrate length is 34 mm.
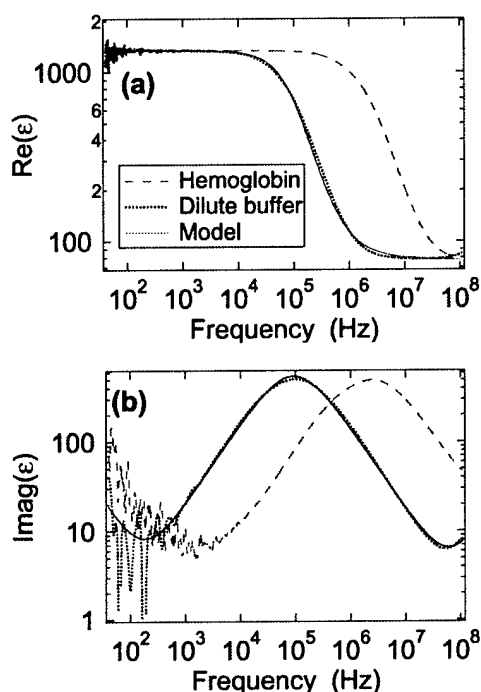
[a)]Electronic mail: gfacer@princeton.edu

FIG. 2. Relative permittivity data: real (a) and imaginary (b) components. Solid traces are from hemoglobin (100 μg/mL), dashed traces for Tris buffer (1 mM, pH 8), and dotted curves are Cole–Cole calculations as per Eq. (1) (parameters $\epsilon_{LF} - \epsilon_{HF} = 1340$, $\tau = 1.70\ \mu$s, $\alpha = 0.91$, and $\sigma_{LF} = 40$ nS).

trodeposited gold layer (total Au thickness 1 μm). The substrate is glass, and connection is via end-launch subminiature (SMA) adaptors. Capacitive coupling to the fluid is achieved by encapsulating the metal lines in 1000 Å of plasma enhanced chemical vapor deposition-grown silicon nitride. Silicone [poly(dimethylsiloxane)] confines the fluid.

At frequencies below $\sim$ 100 MHz, the relative permittivity is obtained from the impedance Z via $\epsilon = 1/j\omega Z C_0$ (C_0 is the capacitance through the sample volume when empty, typically $\sim$ 10 fF). Z data are obtained with a Hewlett-Packard 4294A impedance analyzer (excitation amplitude 500 mV). We have confirmed that the data are free of nonlinear conductive effects. Microwave data ($\geq$45 MHz) are phase-sensitive transmission and reflection coefficients ("S parameters") at the adaptors, obtained with a Hewlett-Packard 8510C vector network analyzer.

We have examined a variety of samples, including solutions of hemoglobin (derived from washed and lysed human red blood cells) and bacteriophage λ-deoxyribonucleic acid (DNA), and live E. coli suspensions. The concentration of hemoglobin is 100 μg/mL in 0.25 M Tris buffer (pH 8), and that of DNA is 500 μg/mL, in 10 mM Tris and 1 mM EDTA (pH 8) buffer. E. coli are suspended in 85% 0.1 M CaCl$_2$/15% glycerol. For the measurements, we have employed both molded microfluidic channels and simpler enclosed wells. Results are consistent (within a scaling factor for the fluid–CPW overlap length) for sample volumes ranging from $\leq$3 pL to $\geq$20 μL. For the following discussions, we present data from capped 10 μL wells.

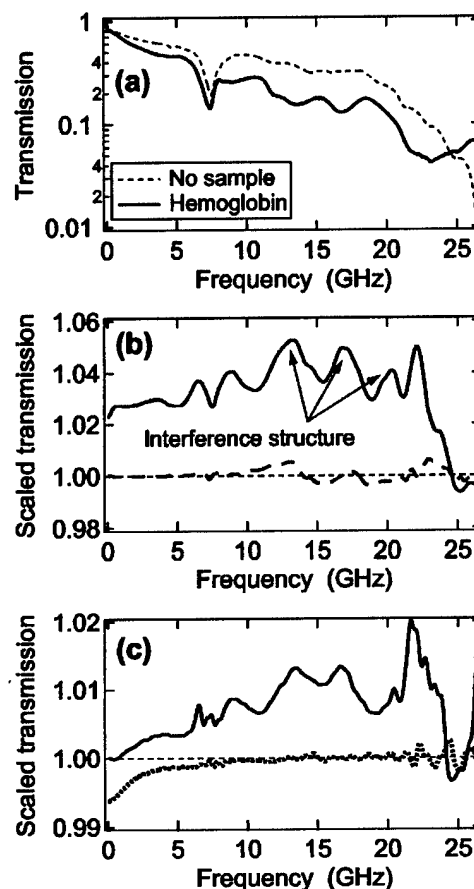Figure 2 shows ϵ from 40 Hz to 110 MHz, for hemoglobin, dilute Tris buffer (concentration 1 mM, pH 8), and a

FIG. 3. Microwave transmission data. (a) Raw data, for the cases of no sample (dotted) and a 100 μg/mL hemoglobin solution (solid). (b) Normalized data (using the respective buffers) for 100 μg/mL hemoglobin (solid trace) and 500 μg/mL phage λ-DNA (dashed), showing the difference in their microwave responses. (c) Solid trace is the (buffer-normalized) response of E. coli, and the dotted trace is that of the Tris buffer from the hemoglobin solution (normalized using deionized H$_2$O).

Cole–Cole[7] model calculation relating ϵ to the angular frequency ω

$$\epsilon = \epsilon_{HF} + \frac{\epsilon_{LF} - \epsilon_{HF}}{1 + (j\omega\tau)^\alpha} - j\frac{\sigma_{LF}}{\omega}. \tag{1}$$

Here $\epsilon_{LF} - \epsilon_{HF}$ is the "dielectric increment," τ is a characteristic time constant, $\alpha \leq 1$ defines the sharpness of the transition, and σ_{LF} is the dc conductivity. For the calculation in Fig. 2, $\epsilon_{LF} - \epsilon_{HF} = 1340$, $\tau = 1.70\ \mu$s, $\alpha = 0.91$, and $\sigma_{LF} = 40$ nS. A small series resistance (90 Ω) is included in the model to fit high-frequency loss within the CPW.

The spectra in Fig. 2 show two features. First, the dielectric increment of the high-frequency transition is a constant of the measurement geometry. Second, and in contrast, the $\epsilon_{LF} \rightarrow \epsilon_{HF}$ transition frequency is directly proportional to the total ionic strength of the solution. As shown, the dispersion model [Eq. (1)] describes the data very well.

Figure 3 shows transmission data from 45 MHz to 26.5 GHz. In Fig. 3(a), raw transmission and reflection are shown for two control cases: a dry sample setup, and deionized water. Figures 3(b) and 3(c) contain transmission data sets for hemoglobin, DNA, and live E. coli which have been normalized with respect to their corresponding buffers. Fig-

ure 3(c) also shows (dotted trace) transmission data from the buffer used for hemoglobin measurements, normalized using deionized water data. This, in particular, demonstrates that even at high salt concentrations (0.25 M Tris-HCl) the microwave effects of buffer salts are limited to a monotonic decrease in transmission below 10 GHz.

Three descriptive notes should be made regarding the data: first, periodic peak and trough features [such as those marked by arrows in Fig. 3(b)] are interference effects due to reflections at the SMA adaptors and the fluid itself. Second, the SMA adaptors impose the high-frequency cutoff at 26.5 GHz. Third, reproducibility of the microwave data has been verified for three CPW devices, using several successive fluidic assemblies on each. Only the interference structure changes slightly from device to device.

The most striking aspect of the microwave data is that the transmission through the hemoglobin and bacteria specimens is higher than that through their respective buffer samples. In addition, the response due to 100 μg/mL of hemoglobin is far stronger than that for DNA, even though the DNA is more concentrated (500 μg/mL). Furthermore, the hemoglobin exhibits increased transmission across a frequency range from <100 MHz to 25 GHz, which is unique among the samples measured to date (by contrast, the onset of increased transmission in the bacteria data is at ≈ 1 GHz). The increases in transmission are not correlated with any change in reflection, indicating that there is a decrease in power dissipation within the sample. Finally, the breadth of the response implies that there is no resonant process at play (as is also the case for the *E. coli* data). We must therefore conclude that the increased transmission represents an increase in the transparency of the medium to microwaves, i.e., that these specimens are "better" dielectrics than water alone at this frequency. The fact that this frequency range coincides with the γ-dispersion transition in water (implying high dissipation) is most likely a contributing factor to the success of detection.

Other samples measured, for which data are not shown here, include collagen, bovine serum albumin, and ribonucleic acid solutions. These macromolecule solutions exhibit behavior highly similar to that of the DNA in Fig. 3(b) (i.e., with the 10–20 GHz interference features present) and *not* to that of the buffer solution. This raises the possibility that the strength and shape of the interference features are more sensitive to the presence of macromolecules and their counterion clouds than just to simple salts. Again, it is reasonable to conclude that this frequency range is significant due to the γ-dispersion of water. The reason for the strength

of transmission enhancement by hemoglobin, compared to that by nucleic acids or other proteins, is yet to be confirmed, but we hypothesize that it is associated with the activity of the central heme complex.

In summary, we have developed coplanar wave guide devices to analyze small volumes of biological samples confined within a microfluidic channel or well. These devices yield permittivity spectra across an exceptionally broad range of frequencies: from 40 Hz to 26.5 GHz thus far. Neither chemical treatment nor surface activation is required. By combining transmission line design with robust thin-film insulation, sensitivity to sample properties can be achieved in both low- and high-frequency regimes within a single device. We observe transmission enhancements, with different frequency dependences, for hemoglobin solutions and suspensions of *E. coli* bacteria.

[1] S. Nie and R. N. Zare, Annu. Rev. Biophys. Biomol. Struct. **26**, 567 (1997).
[2] S. Weiss, Science **283**, 1676 (1999).
[3] G. MacBeath and S. L. Schreiber, Science **289**, 1760 (2000).
[4] J. Viovy, Rev. Mod. Phys. **72**, 813 (2000).
[5] L. L. Sohn, O. A. Saleh, G. R. Facer, A. J. Beavis, R. S. Allan, and D. A. Notterman, Proc. Natl. Acad. Sci. U.S.A. **97**, 10687 (2000).
[6] H. Fricke, Philos. Mag. **14**, 310 (1932).
[7] K. S. Cole and R. H. Cole, J. Chem. Phys. **9**, 341 (1941).
[8] K. Asami, E. Gheorghiu, and T. Yonezawa, Biophys. J. **76**, 3345 (1999).
[9] C. Prodan and E. Prodan, J. Phys. D **32**, 335 (1999).
[10] G. Smith, A. P. Duffy, J. Shen, and C. J. Olliff, J. Pharm. Sci. **84**, 1029 (1995).
[11] H. E. Aylife, A. B. Frazier, and R. D. Rabbitt, IEEE J. Microelectromech. Syst. **8**, 50 (1999).
[12] J. Hefti, A. Pan, and A. Kumar, Appl. Phys. Lett. **75**, 1802 (1999).
[13] J. M. Cooper, Trends Biotechnol. **17**, 226 (1999).
[14] D. C. Duffy, J. C. McDonald, O. J. A. Schueller, and G. M. Whitesides, Anal. Chem. **70**, 4974 (1998).
[15] H. P. Schwan and S. Takashima, *Encyclopedia of Applied Physics* (VCH, New York, 1993), Vol. 5, pp. 177–200.
[16] P. Debye, *Polar Molecules* (Dover, New York, 1929).
[17] G. De Gasperis, X. Wang, J. Yang, F. F. Becker, and P. R. C. Gascoyne, Meas. Sci. Technol. **9**, 518 (1998).
[18] A. K. Jonscher, Nature (London) **267**, 673 (1977).
[19] B. Onaral, H. H. Sun, and H. P. Schwan, IEEE Trans. Biomed. Eng. **31**, 827 (1984).
[20] P. A. Cirkel, J. P. M. van der Ploeg, and G. J. M. Koper, Physica A **235**, 269 (1997).
[21] J. Gimsa and D. Wachner, Biophys. J. **75**, 1107 (1998).
[22] V. Raicu, Phys. Rev. E **60**, 4677 (1999).